

UTRECHT UNIVERSITY

MASTER THESIS

**Exploration of ocean mechanical
geoengineering alternatives: effect of
diapycnal mixing enhancement on the
ocean uptake of atmospheric CO₂**

Author:
Federica CASTINO

Supervisors:
prof. dr. ir. H. A. Dijkstra
dr. T. van Leeuwen

Institute for Marine and Atmospheric research Utrecht
Department of Physics, Utrecht University, Utrecht, the Netherlands

31st July 2020

UTRECHT UNIVERSITY

Abstract

Institute for Marine and Atmospheric research Utrecht
Department of Physics, Utrecht University, Utrecht, the Netherlands

Master of Science

Exploration of ocean mechanical geoengineering alternatives: effect of diapycnal mixing enhancement on the ocean uptake of atmospheric CO₂

by Federica CASTINO

Many ocean-based geoengineering techniques have been suggested to improve the efficiency of the “biological pump”. Alternatively, in this study we investigate how enhancing diapycnal mixing at specific locations would affect all the forcings that influence the ocean carbon uptake, on decadal time scales. Firstly, we use the Oceanic General Circulation Model (OGCM) of the CSIRO Mk3L Climate System Model, in order to observe the response of the ocean to variations in the parameterization of the vertical diffusivity K_v . This version of the CSIRO Mk3L model is combined with the COAL (Carbon of the Ocean, Atmosphere and Land) component to represent the carbon cycle, nutrient cycling and organic matter cycling in the ocean. In our experiments, the model can also estimate the power added to the system in order to obtain a highly mixed model column. Subsequently, we combine the OGCM with the NOMAD (Nonlinear Optimization by Mesh Adaptive Direct Search) software, with the aim of identifying the locations where a higher K_v would lead to a decline in the partial pressure of CO₂ at the ocean surface on short time scales. Lastly, we test our hypothesis using a Community Earth System Model (CESM) that includes the simulation of the global carbon cycle, in order to analyse the combined response from the oceanic, atmospheric and terrestrial components.

Contents

| | |
|--|------------|
| Abstract | iii |
| 1 Introduction | 1 |
| 1.1 Complex Systems Research Project | 2 |
| 2 Methods | 3 |
| 2.1 Ocean response to a global variation in diapycnal mixing | 3 |
| 2.1.1 Representation of vertical diffusivity in the OGCM | 3 |
| Biogeochemical component | 4 |
| Estimate of the energy required for artificial mixing | 5 |
| Experimental design | 5 |
| 2.2 Artificial mixing hotspots: optimization problem | 6 |
| 2.2.1 Experimental design | 6 |
| 2.3 CESM experiments | 7 |
| 2.3.1 Representation of vertical mixing in the CESM | 7 |
| 3 Results | 9 |
| 3.1 Air-sea CO ₂ flux map in the model mean state | 9 |
| 3.2 Global mixing experiments | 10 |
| 3.3 Global hotspots experiments | 12 |
| 3.4 Optimization problem results | 13 |
| 3.5 CESM hotspots experiments | 15 |
| 3.6 CESM regional experiments | 17 |
| 3.6.1 Increased K_v in the Equatorial Atlantic and Mediterranean Sea | 19 |
| 3.6.2 Increased K_v in the Northwestern Atlantic | 21 |
| 4 Discussion | 23 |
| 4.1 Estimate of the power required to increase K_v | 23 |
| 4.2 Optimization procedure | 23 |
| 5 Conclusion | 25 |
| A The optimization problem | 27 |
| A.1 The MADS algorithm | 27 |
| A.2 <i>SGTELIB</i> library | 29 |
| A.3 Definition of the optimization problem | 29 |
| A.4 The blackbox | 30 |
| B Additional Figures | 33 |
| B.1 Global mixing experiments with the OGCM | 33 |
| B.2 Global hotspots experiments with the OGCM | 37 |
| B.3 CESM simulations: regional experiments | 39 |
| B.3.1 EQATL_MED experiment | 39 |
| B.3.2 NWATL experiment | 39 |

List of Abbreviations

| | |
|------------------|--|
| CSIRO | Commonwealth Scientific and Industrial Research Organization |
| CESM | Community Earth System Model |
| OGCM | Ocean General Circulation Model (included in CSIRO Mk3L model) |
| AGCM | Atmospheric General Circulation Model (included in CSIRO Mk3L model) |
| COAL | Carbon of the Ocean, Atmosphere and Land |
| OBGCM | Ocean Biogeochemical Model |
| NOMAD | Nonlinear Optimization by Mesh Adaptive Direct Search software |
| MADS | Mesh Adaptive Direct Search algorithm |
| GPS | General Pattern Search algorithms |
| SGTELIB | Surrogate Library for NOMAD |
| CTRL | Control run |
| EQATL_MED | Equatorial Atlantic and Mediterranean Sea configuration |
| NWATL | NorthWestern Atlantic configuration |
| DIC | Dissolved Inorganic Carbon |
| POC | Particulate Organic Carbon |
| PIC | Particulate Inorganic Carbon |
| (A)MOC | (Atlantic) Meridional Overturning Circulation |
| SST | Sea Surface Temperature |
| SSS | Sea Surface Salinity |

Frequently used Symbols

| | |
|---------------|--|
| pCO_2^{oce} | partial pressure of CO ₂ at the ocean surface |
| pCO_2^{atm} | partial pressure of CO ₂ in the atmosphere |
| K_v | oceanic diapycnal diffusivity |

Chapter 1

Introduction

Variations in air-sea fluxes of heat, water, and carbon dioxide can affect the Earth climate on seasonal to millennial time scales (Matear and Hirst, 1999; Riebesell, Rtzinger and Oschlies, 2009). In particular, during the last decades, the ocean has played a crucial role in regulating the concentration of CO₂ in the atmosphere, as stated in the Special Report on the Ocean and the Cryosphere in a Changing Climate (SROCC, Pörtner et al., 2019). According to this Report, 20 – 30 % of the anthropogenic CO₂ emitted in the last four decades has been absorbed by the ocean. As a direct consequence, the oceanic carbon uptake has moderated the rate of global warming. Moreover, ocean currents affect continental temperatures, being responsible for the transport of heat from low to high latitude. Since the terrestrial carbon pool is highly sensitive to temperature variations (Luo, 2007), the ocean also has an impact on the amount of carbon stored by terrestrial vegetation and soil.

Considering the crucial role of the ocean in controlling the Earth climate, ocean-based carbon dioxide removal techniques have been advanced to reduce the effects of the anthropogenic CO₂ emissions. Previous studies suggested that they would have the potential to effectively mitigate Climate Change at a global scale (Zhang et al., 2015). These techniques are a subset of a larger group of geoengineering methods, which have been proposed to counteract the causes or the effects of Climate Change. Methods of geoengineering rely on the deliberate manipulation of the Earth Climate, for example by varying the amount of solar radiation reaching the planet surface. The implementation of some of these techniques might cause dangerous side effects, which are difficult to evaluate due to the complexity of the climate system (Zhang et al., 2015). On the other hand, the development and implementation of geoengineering methods might be necessary to keep the global warming below 1.5°C, since most mitigation pathways imply reliance on net negative CO₂ emissions (Rogelj et al., 2018). For this reason, the importance of investigating complementary solutions for climate change mitigation, such as ocean-based geoengineering methods, should not be underestimated.

Ocean-based geoengineering techniques usually address the efficiency of the so called *biological pump*. The *biological pump* is the main mechanism responsible for the transport of carbon from the ocean surface to its interior, through sinking of organic matter. This *pump* is affected by variations in the amount of nutrients and temperature in the ocean surface. A more efficient *biological pump* leads to lower concentrations of dissolved inorganic carbon (DIC) in surface waters. As a consequence, at the surface, the partial pressure of CO₂ ($p\text{CO}_2^{\text{ce}}$) is reduced, and the ocean carbon uptake is enhanced. For example, the ocean iron fertilization is among the most discussed geoengineering proposals (Aumont and Bopp, 2006). This method involves adding iron to surface waters to intensify the marine biological activity and, as a consequence, the ocean carbon uptake.

Alternative proposals to fertilize the ocean surface suggest to increment the upwelling of nutrients from deep waters by mechanical means (Dutreuil, Bopp and Tagliabue, 2009; Oschlies et al., 2010).

However, variations in ocean circulations and mixing would affect not only the biological pump, but also a second mechanism, the *solubility pump*. At specific locations, this second mechanism can be the dominant process controlling the air-sea CO_2 flux, since it includes the effects on the oceanic carbon cycle due to variations in the vertical profiles of temperature, DIC concentration and alkalinity. It is particularly easy to quantify the effect of a temperature variation on the solubility of CO_2 in the ocean, since it is well known that a cooling of 1°C causes a 4% decrease in the $p\text{CO}_2^{\text{oce}}$ (Takahashi et al., 1993). Hereinafter we will refer to these processes as *thermodynamic* and *hydrodynamic forcing* on the air-sea CO_2 flux. This terminology is used to specify how a variation in ocean circulation and mixing affects the ocean carbon uptake (Fasham, 2003).

Variations in ocean upwelling and diapycnal mixing are likely to have significant impacts on the Earth climate on short time scales (Oschlies et al., 2010; Dutreuil, Bopp and Tagliabue, 2009). The response of the carbon cycle is due to local consequence on the vertical profiles of temperature and DIC concentration, as well as non-local effects, for example the advection of alkalinity anomalies (Dutreuil, Bopp and Tagliabue, 2009).

In this project, we will test the hypothesis that the artificial enhancement of diapycnal diffusivity K_v in specific regions of the ocean can lead to an increase in the ocean uptake of anthropogenic CO_2 .

This hypothesis is supported by observations: for example, it was suggested that periods of intense vertical mixing can lead to an increase in ocean carbon uptake in the Mediterranean Sea, as it was observed in the winter of 1999 (Copin-Montégut and Bégovic, 2002)

With this study, we conduct and analyse climate model simulations to evaluate the effects of increasing K_v . Moreover, we quantify the power that would be required to implement this geoengineering method. We use two climate models: the Commonwealth Scientific and Industrial Research Organisation Mark 3L (CSIRO Mk3L) climate system model, and the Community Earth System Model (CESM) version 1.0.5, which are described in Chapter 2.

Moreover, we define and solve an optimization problem, with the aim of identifying the locations where an increased K_v can lead to an increment in the oceanic carbon uptake (*Complex Systems Research Project*, see Section 1.1).

1.1 Complex Systems Research Project

In this report, we combine the description of the Climate Physics master thesis and of the Complex Systems research project. In particular, the Complex Systems research part consists in the resolution of the optimization problem, which is illustrated in Section 2.2, 3.4, 4.2 and in the Appendix A.

Chapter 2

Methods

In this Chapter, we describe the methods used to test our hypotheses. Firstly, we illustrate how we test the ocean response to a global variation in K_v (Section 2.1). Subsequently, we present our approach to solve the optimal placement problem (Section 2.2). Lastly, we summarize the characteristics of the CESM version used to examine specific configurations (Section 2.3).

2.1 Ocean response to a global variation in diapycnal mixing

We study the response of the ocean to global variations in diapycnal mixing using the Ocean General Circulation Model (OGCM) of the CSIRO Mark3L climate system model, which is a low-resolution version of the CSIRO Mk3 model.

In the following paragraphs, we summarize the main features of the OGCM, which is described in detail in Phipps, 2010.

The ocean is represented by 21 vertical layers with nonuniform thickness, which ranges from 25 m at the surface to 450 m at the bottom. The model horizontal resolution is 2.8125° EW \times $\sim 1.59^\circ$ NS. The resolution of the continental land mask is lower, since it was generated to be compatible with both the OGCM and the Atmospheric General Circulation Model (AGCM) included in the fully coupled CSIRO Mk3 model. The resolution of the AGCM is 5.625° EW \times $\sim 3.18^\circ$ NS, so that 4 oceanic grid-boxes correspond to one atmospheric grid-box.

When the model is run in the stand-alone ocean mode, auxiliary files are required to define the upper boundary conditions. Those files must contain the monthly values of salinity (SSS), temperature (SST) and wind stress at the sea surface. A timescale of 20 days is set for the relaxation of temperature and salinity in the model upper layer towards the prescribed SST and SSS.

The model spin-up run is conducted under pre-industrial conditions: in particular, the atmospheric CO_2 concentration is set to a constant value of 280 ppm. The initial ocean state and boundary conditions are derived from the World Ocean Atlas 1998 (*National Oceanographic Data Center, Ocean Climate Laboratory Products*).

2.1.1 Representation of vertical diffusivity in the OGCM

In our experiments, we modify the parameterization of the vertical diffusivity K_v in the OGCM. Therefore, it is important to examine how the background K_v is represented in the model.

The vertical ocean mixing follows the scheme by Gargett A.E., 1984. According to this study, K_v can be parameterized as a function of the Brunt-Väisälä frequency N , following the profile:

$$K_v(i, j, k) = \frac{a_o}{N(i, j, k)} \quad (2.1)$$

where i, j, k identify the horizontal and vertical position of the model ocean box, and a_o is a parameter depending on the rate at which the energy is passed to small scales by internal waves. In this model, $a_o = 10^{-3} \text{ cm}^2 \text{ s}^{-2}$ for the oceanic internal wave field.

Moreover, to mimic wind-forced mixing, a minimum value of K_v is imposed between the upper two levels - where $K_{v,min}(i, j, 2) = 2 \times 10^{-3} \text{ m}^2 \text{ s}^{-1}$ - and between the second and third levels - $K_{v,min}(i, j, 3) = 1.5 \times 10^{-4} \text{ m}^2 \text{ s}^{-1}$. At deeper levels, the minimum value of K_v is set to a value that is an order of magnitude lower - $K_{v,min}(i, j, k) = 3 \times 10^{-5} \text{ m}^2 \text{ s}^{-1}$.

In case of static instability, the value of K_v is raised to $100 \text{ m}^2 \text{ s}^{-1}$, in order to simulate convective mixing.

In our experiments, the value of K_v from Equation 2.1 will be incremented by $10^{-4} \text{ m}^2 \text{ s}^{-1}$ in the ocean grid-boxes where we simulate the employment of mechanical mixers, in order to achieve a highly mixed ocean column. This value has already been used in other ocean models to represent natural hotspots of vertical mixing: for example, a similar value of K_v was suggested for the representation of diapycnal diffusivity in the Java, Flores, and Banda Seas by Jochum and Potemra, 2008. According to this study, the Indonesian marginal seas are sites of elevated mixing, due to the breaking of internal tides and strong ocean currents flowing over sills. Analogous estimates of diapycnal mixing from these processes were obtained in the proximity of the Mascarene Plateau (Lozovatsky, 2003), which is also characterized by intense internal waves activity due to the local bathymetry. Moreover, the presence of natural sites with K_v in the order of $10^{-4} \text{ m}^2 \text{ s}^{-1}$ was linked to increased biomass in the Northern Bay of Biscay (Pingree and New, 1995).

Biogeochemical component

The CSIRO Mk3L model can be combined with the Carbon of the Ocean, Atmosphere and Land (COAL) biogeochemical model, in order to represent the evolution of carbon, nitrogen and phosphorus in the atmosphere and in the ocean. The ocean biogeochemical component (OBGCM) also represents alkalinity, oxygen and iron cycles.

The equation used to model the OBGCM tracers are described in Matear and Lenton, 2014. Of particular interest for this project is the conservation equation for dissolved inorganic carbon (DIC). Its evolution in time is described by:

$$\frac{\partial DIC}{\partial t} = -\nabla_3(uDIC) + \nabla_I(K_I \nabla_I DIC) + \frac{\partial}{\partial z} \left(K_v \frac{\partial DIC}{\partial z} \right) + Q_F^{DIC} - Q_O^{DIC} - Q_I^{DIC} \quad (2.2)$$

where the terms on the r.h.s. represent advection, diffusion along isopycnal surfaces, diapycnal diffusivity, flux across the air-sea interface, particulate organic carbon (POC) production and consumption, and particulate inorganic carbon (PIC) production and dissolution.

Therefore, a variation in K_v affects the evolution of DIC directly, through the vertical mixing term in Equation 2.2, and indirectly, via variations in the fluxes Q_F^{DIC} , Q_O^{DIC} and Q_I^{DIC} .

In the Results section (Chapter 3), we will look in particular at the changes in the carbon surface flux Q_F^{DIC} , which is parameterized as:

$$Q_F^{DIC} = K_g(pCO_2^{atm} - pCO_2^{oce}) \quad (2.3)$$

where K_g is the gas exchange coefficient, while pCO_2^{atm} and pCO_2^{oce} represent the partial pressure of CO_2 in the atmosphere and at the ocean surface, respectively. In our experiments with the CSIRO model, $pCO_2^{atm} = const. = 280$ ppm. Therefore, a necessary condition for increasing in the ocean carbon uptake is to reduce the value of pCO_2^{oce} .

Estimate of the energy required for artificial mixing

We want to understand what is the order of magnitude of the power required to increment K_v by $10^{-4} m^2 s^{-1}$. To have a reference value to which compare our estimates, we will consider the amount of power that could be collected by installing ocean turbines. This would be a clean energy source, and it could be generated close to the site where the artificial mixers are installed.

We assume that the length scale L at which the artificial mixers transmit turbulent kinetic energy to the ocean water is larger than the Ozmidov length scale:

$$L_O = \sqrt{\epsilon/N^3}$$

where ϵ is the rate of turbulent energy dissipation, while N is the Brunt-Väisälä frequency. This assumption allows us to assume that the mixing efficiency Γ approaches its maximum value: $\Gamma_{max} = 0.2$ (Bluteau, Jones and Ivey, 2013).

In this case, it is possible to estimate the energy required for artificial mixing using the following equation (Osborn, 1980):

$$\epsilon(z) = \frac{K_v}{\Gamma} N^2(z) \sim \frac{K_v}{0.2} N^2(z) \quad (2.4)$$

where $N(z)$ is the Brunt-Väisälä frequency, and where we assume an optimal mixing efficiency $\Gamma \sim 0.2$.

Lastly, the power required to increase K_v in the ocean grid-box i, j, k is obtained including in the OGCM the following calculation:

$$P(i, j, k) = \epsilon(i, j, k)M(i, j, k) = \frac{10^{-4} m^2 s^{-1}}{0.2} N^2(i, j, k)M(i, j, k)$$

where $M(i, j, k)$ is the mass of the ocean grid-box, and $\epsilon(i, j, k)$ is the rate of turbulent energy dissipation, which is calculated using Equation 2.4.

Experimental design

The OGCM will be used to study the response of the ocean to variations in diapycnal mixing, and to find the optimal configuration of a potential implementation of artificial enhancement of vertical diffusivity.

First of all, we need to test the sensitivity of the model to changes in diapycnal mixing. Therefore, we run experiments starting from a condition of equilibrium, and we look at the time scale of the response of the system. The model was spun up under preindustrial atmospheric CO₂ concentration, which is defined to be constant and set at 280 ppm, until the simulated climate became stable. We start our experiments from this condition of equilibrium, and we perturb the system increasing the vertical diffusivity at every ocean column (Section 3.2) or at specific locations (Section 3.3).

We will run 50 year simulations, in which artificial mixing starts after 5 years, and it continues constantly for the following 45 years.

In the following paragraph (Section 2.2), we explain how the OGCM is coupled to the NOMAD optimization software, in order to identify the most suitable locations for the implementation of this geoengineering technique.

2.2 Artificial mixing hotspots: optimization problem

Since geoengineering methods are more likely to be implemented over a restricted area of the ocean, it is interesting to investigate which is the *optimal choice* for the artificial mixer placement, i.e. *the solution leading to the minimum value of global mean pCO₂^{oce}*. Moreover, this analysis can lead to a better understanding of the non-local effects that hotspots of diapycnal mixing have on the ocean carbon cycle.

For this analysis, we couple the ocean component of the CSIRO Mk3L climate model to the Nonlinear Optimization by Mesh Adaptive Direct Search (NOMAD) software. This model implements the Mesh Adaptive Direct Search (MADS) algorithm to solve computationally expensive optimization problems (Le Digabel et al., 2009).

The aim of the algorithm is to improve the current best feasible solution, using the information collected in the previous model evaluations. At each iteration, a 5-year simulation of the OGCM is completed. All the scripts needed to generate the model input, run the simulation, and process the model output, are included in a so-called *blackbox*: this program is able to read as input the new potential solution x suggested by the NOMAD software, and it gives as output the value of the objective function $f(x)$ at that point. Since the computational cost of one blackbox evaluation is very high, we also use dynamical surrogate functions: this method involves the use of the information collected in the previous model runs, to approximate the real objective function $f(x)$ with a surrogate $s(x)$. This allows us to apply a preliminary test on the potential trial points.

Appendix A contains a more detailed description of the methods that were used in this section of the project.

2.2.1 Experimental design

The MADS algorithm and the blackbox (or surrogate function) are evaluated in a loop until either the maximum number of blackbox evaluations, or the maximum running time, is reached. The input file to the NOMAD algorithm is used to indicate the specific properties of each experiment. We set the maximum time for the model evaluation at 4 days, and no more than 300 evaluations can be performed. Moreover, we can specify that each pair of variable represents the coordinates of one location, so that the algorithm generates the new trial points by moving one location at a time. This technique is typically used in optimal placement problems (Alarie et al.,

2013). We test our method under different initial solutions, problem dimensions, and search regions, as it is described in Sections 3.4, and in the Appendix A.

2.3 CESM experiments

The CESM 1.0.5 will be used to test some potential configurations of mixing hotspots.

We use a version of the model that includes a biogeochemical component, so that the carbon cycle in the Earth System is simulated.

We run 140 years simulations, starting from an initial condition similar to the one described in Section 2.1, meaning that the model spin-up run is performed under preindustrial condition. At year 40 of our model run, two branches are simulated: a control run (CTRL) and a simulation in which K_v is incremented in specific regions of the ocean for the following 100 years. We test 5 configurations: 3 hotspots experiments (*Ind*, *Alt3*, and *Atl6*) and 2 regional experiments (EQATL_MED and NWATL).

The sites of enhanced mixing in each experiment are indicated in Figures 3.5 and 3.8.

2.3.1 Representation of vertical mixing in the CESM

In the CESM model, the background vertical diffusivity follows the vertical profile in Bryan and Lewis, 1979, which is given by the following expression:

$$K_v(z) = K_{v,1} + K_{v,2} \times \arctan[(|z| - d) \times l_{inv}] \quad (2.5)$$

where $K_{v,1}$ is the value of K_v at $|z| = d$, while $K_{v,2}$ determines the amplitude of the variation of K_v in the water column, and l_{inv} is the inverse length-scale of the transition region (Smith et al., 2010).

The values assigned to the parameters included in Equation 2.5 lead almost everywhere to a typical value of vertical diffusivity: $K_v \sim 0.17 \times 10^{-4} \text{ m}^2 \text{ s}^{-1}$. However, a latitudinal structure is also included, by increasing K_v in the latitude bands around 30° N/S to $K_v = 0.3 \times 10^{-4} \text{ m}^2 \text{ s}^{-1}$, while at the equator it is reduced to $K_v = 0.1 \times 10^{-4} \text{ m}^2 \text{ s}^{-1}$. Moreover, a natural site of intense vertical mixing is simulated in the Banda Sea, where $K_v = 1.0 \times 10^{-4} \text{ m}^2 \text{ s}^{-1}$.

In our experiments, we set the same value $K_v = 1.0 \times 10^{-4} \text{ m}^2 \text{ s}^{-1}$, from the surface of the ocean until a depth $z = 1000 \text{ m}$, at all the locations where we simulate the employment of artificial mixers as a geoengineering technique.

Chapter 3

Results

In this Chapter, we present the main results of our project. The effect of increasing K_v on the carbon cycle will be measured through the observed variation in the partial pressure of CO_2 at the ocean surface ($p\text{CO}_2^{\text{oce}}$): in fact, a necessary condition to obtain an increase in the uptake of CO_2 is to reduce the global mean $p\text{CO}_2^{\text{oce}}$.

Firstly, we briefly describe the spatial distribution of $p\text{CO}_2^{\text{oce}}$ in the model mean state, in order to highlight which are the main natural oceanic sources and sinks of CO_2 to the atmosphere (Section 3.1). Then, we look at the experiments conducted with the OGCM of the CSIRO Mk3L-COAL model (Section 3.2 and 3.3). Lastly, we describe the outcome of the optimization problem (Section 3.4), and we analyse the output of the CESM simulations (Section 3.5 and 3.6).

3.1 Air-sea CO_2 flux map in the model mean state

As we described in Section 2.1 (see Equation 2.3), the carbon surface flux Q_F^{DIC} is proportional to the difference $\Delta p\text{CO}_2$ between the partial pressure of CO_2 in the ocean surface and in the atmosphere: $\Delta p\text{CO}_2 = p\text{CO}_2^{\text{oce}} - p\text{CO}_2^{\text{atm}}$.

Figure 3.1 shows the spatial distribution of $\Delta p\text{CO}_2$ in the CSIRO Mk3L-COAL model mean state. This plot is obtained from a 5 year average of the model conditions at the end of the spin-up run.

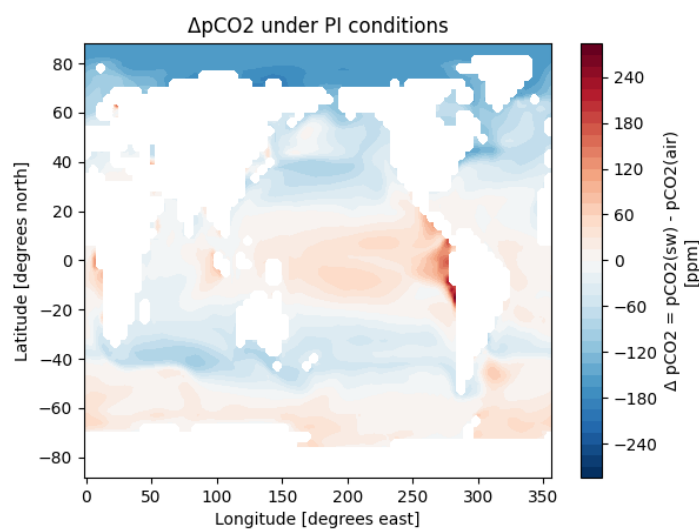


FIGURE 3.1: Distribution of $\Delta p\text{CO}_2$ under pre-industrial (PI) conditions - averaged over 5 years of the OGCM control simulation.

Looking at Figure 3.1, we can see the main features characterizing the global pattern of the air-sea CO_2 flux. One can observe that the main sources of CO_2 to the atmosphere are regions where the *hydrodynamic forcing* is dominant, i.e. regions where the upwelling of deep water leads to higher concentrations of DIC in the ocean surface. In particular, we can see that the upwelling regions at the equatorial divergence and in the Southern Ocean are characterized by $p\text{CO}_2^{\text{oce}} > p\text{CO}_2^{\text{atm}}$.

Moreover, in the Eastern Equatorial Pacific, other two factors contribute to the CO_2 outgassing: the deep water is highly heated when it reaches the surface, and the biological activity is limited by the availability of nutrients in the area. As a result, the *thermodynamic* and *biological forcings* are also responsible for the high values of $p\text{CO}_2^{\text{oce}}$ registered there. The net effect of increasing K_v in this region is difficult to predict: on one hand, more carbon would reach the ocean surface; on the other hand, it might reduce the surface temperature and increment the amount of nutrients, leading to a beneficial effect through both the solubility and the biological pumps. The complex interaction between these opposite responses will determine the final outcome.

Other sensitive regions are the western boundary currents, which represent the major sinks of atmospheric carbon in the ocean. In particular, along the Kuroshio current and the Gulf Stream, the warm waters lose heat while they are transported northward. As a result, these regions are characterized by a net under saturation of CO_2 (Fasham, 2003). Increasing K_v at - or close to - these regions, we can expect consequences both on local scales and in the whole basin, through potential changes in the Meridional Overturning Circulation (MOC).

3.2 Global mixing experiments

In this Section, we present the results from the first experiments with the OGCM running in stand-alone mode: therefore, the boundary conditions at the air-sea interface do not vary in time. In these experiments, we enhance vertical mixing globally: K_v is higher by $1 \times 10^4 \text{ m}^2\text{s}^{-1}$ at every ocean model column. Two possibilities are considered, in which artificial mixers are employed (1) from the ocean surface or (2) from a depth of about 200 m (the 7th model layer). In both cases, K_v is increased until $z = 1000 \text{ m}$ (the 12th model layer). Note that artificial mixing starts from year 5 of the simulation, and then it continues constantly for the following 45 years.

With these experiments, we want to test the sensitivity of the system to a global variation of K_v : therefore, we are interested in the magnitude of the variation in $p\text{CO}_2^{\text{oce}}$, the timescales involved in its evolution, and the power added to the system to increase K_v by $1 \times 10^4 \text{ m}^2\text{s}^{-1}$. These data can be obtained looking at the two plots in Figure B.1 and B.2, which show the first 20 years of employment of artificial mixers.

The most important conclusion that we can deduce from Figure B.1 is that, in both experiments, a global increment of K_v leads to an increase in the global mean value of $p\text{CO}_2^{\text{oce}}$. When the geoengineering method is implemented from the ocean surface, the magnitude of the increase in $p\text{CO}_2^{\text{oce}}$ is $\sim 14 \text{ ppm}$, while in the second scenario it is about 4 ppm. Both curves reach a plateau before the end of the simulation, showing that the mechanisms involved can lead to a new stability between the atmosphere and the ocean surface in the time scales of our experiment, when the atmospheric conditions are kept constant.

Figure B.2 shows the global mean vertical profile of the power added to the system, to obtain a $1 \times 10^4 \text{ m}^2 \text{ s}^{-1}$ increase in the diapycnal mixing. The values shown are relative to the average power needed for one model column. Integrating over the whole column, we find that the total power needed for one model column ranges from $P_{tot} = 425 \text{ MW}$ (starting from the surface) to $P_{tot} = 179 \text{ MW}$ (starting from $z = 200 \text{ m}$). Dividing by the mean area covered by one model column, we find that the average power added to the system is 7.7 kW km^{-2} and 3.2 kW km^{-2} in the two scenarios, respectively.

However, further studies are needed to verify the assumptions that we made in our calculations, most importantly the assumption of approaching the optimal mixing efficiency Γ_{max} : the value of Γ depends on the length scales at which the energy is passed to the system (see Section 2.1) and, therefore, on the technology employed to obtain the increase in K_v .

Unless differently specified, hereafter we will always consider experiments in which the artificial mixers operate from the surface of the ocean, in order to obtain a larger response from the ocean.

Figure B.3 shows the spatial pattern of the $\Delta p\text{CO}_2$ variation, and its evolution in time. Regions where $\Delta p\text{CO}_2$ increases indicate a harmful effect on the oceanic carbon uptake, while a decrease of $\Delta p\text{CO}_2$ is linked to a beneficial effect on the efficiency of the carbon pumps.

Firstly, one can observe that the maximum amplitude of the increase in $\Delta p\text{CO}_2$ is larger than the maximum reduction, and that harmful effects occur over large regions of the ocean. These two first considerations are in agreement with what observed in Figure B.1, i.e. that the global mean variation in $p\text{CO}_2$ is positive. Moreover, the spatial pattern is approximately constant after the first few years, and in the following part of the simulation both positive and negative effects amplify their magnitude over time: we can interpret this observation with the fact that, in general, the relative impact of the three forcings at a specific location do not vary in time. This explains why the global mean value reaches a plateau in Figure B.1.

Only specific areas show a large reduction in $\Delta p\text{CO}_2$: for example, the region along the western coastline of North America is characterized by a lower $\Delta p\text{CO}_2$ in the experiment compared to the mean state of the model, with a variation in the order of -40 ppm .

To better understand the mechanisms leading to these results, one can look at the maps in Figure B.4. This Figure highlights only the areas where beneficial effects were observed, i.e. where we obtained a decrease in $\Delta p\text{CO}_2$ (Figure B.4a and B.4b), SST (Figure B.4c and B.4d), or Sea Surface DIC concentration (Figure B.4e and B.4f). We can observe that, after one year of artificial mixing, the dominant forcing over large regions of the Global Ocean seems to be the thermodynamic forcing: a reduced SST is registered almost everywhere, due to the upwelling of deep colder water. However, by the end of the simulation, the regions characterized by a lower SST do not correspond to the areas with lower values of $p\text{CO}_2^{occe}$. Therefore, we can conclude that the interplay between the hydrodynamic and the biological forcings appears to be responsible for a potential increase in the ocean carbon uptake on longer timescales.

The biological pump is responsible for the sinking of carbon to deeper waters, via the production of Particulate Organic Carbon (POC). To verify if this process was amplified by the artificial increase of K_v , we look at the variation of the POC

production in Figure B.5 (note that these three maps are relative to year 20 in the simulation where mixing is increased from a depth of $z = 200$ m). In Figure B.5a, we can detect two large areas where the ΔpCO_2 reduction is in the order of magnitude of 10 ppm, one located at the center of the Pacific Ocean, in the Southern Hemisphere, and one in the Atlantic Ocean, covering the Equatorial Atlantic and extending southward along the east coast of South America: looking at Figure B.5b, we can attribute the largest pCO_2^{oce} reduction in the Pacific Ocean to an increment in the POC production, caused by an intensified biological activity; it is more difficult to understand the drivers of the pCO_2^{oce} reduction in the Atlantic Ocean, which could be linked to a lower SST in the basin (Figure B.5c) and effects on the meridional overturning circulation.

3.3 Global hotspots experiments

In this Section, we increase K_v by $1 \times 10^4 \text{ m}^2\text{s}^{-1}$ in the upper 12 levels of the CSIRO Mk3L-COAL ocean model, at 1 ocean column every N_{col} model grid cells in the latitudinal and longitudinal direction: therefore, we tested here the effects of having specific sites of intense vertical mixing (hotspots), that are evenly distributed within the Global Ocean.

With these experiments, we want to test which are the main non local effects caused by an artificial enhancement of diapycnal mixing, similarly to what was done in Dutreuil, Bopp and Tagliabue, 2009.

In the case $N_{col} = 4$, the locations where K_v was incremented are indicated in Figure 3.2.

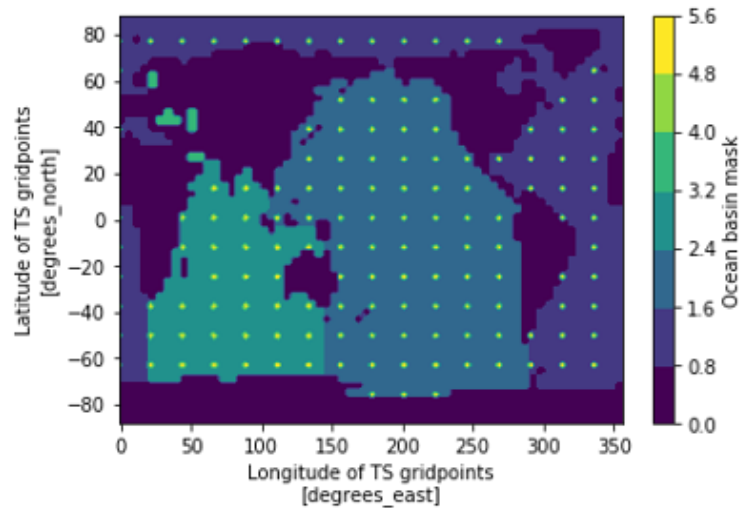


FIGURE 3.2: Locations of the sites where K_v is incremented (yellow dots) from the ocean surface to $z = 1000$ m.

The experiment results can be found in Figures B.6 and B.7.

The intensity of the variation in ΔpCO_2 (Figure B.6) is an order of magnitude lower than the one obtained in the global mixing experiment (Figure B.3). We can also observe that the variation is generally more intense at the artificial mixing site, with some exceptions, the most evident being in the Eastern Equatorial Pacific: here, relatively large effects are also detectable at locations where K_v had the same value as in the control run.

Similarly, in Figure B.7 we can see that the potential reductions in SST and DIC concentration can be registered also because of the advection of anomalies generated at the mixing hotspots to areas where K_v remained unchanged. Especially after the first simulation years, when the results start to stabilize, the extension and location of the areas that benefit from the geoengineering technique is similar to the one found in the Global Mixing Experiment (Section 3.2), as we can deduce comparing Figure B.4b and Figure B.7b.

3.4 Optimization problem results

In this section, we present the results obtained from the resolution of the optimization problem, in which we aim to find the best locations where to increase vertical mixing.

The efficiency of the MADS algorithm depends on two main factors: the search region and the dimension of the problem.

First of all, we fix the number of mixing location to $n = 3$, and we compare the results obtained using different domains. In particular, we considered four potential search regions: the Atlantic, Pacific, Indian and Global Ocean. The resolution of the grid is such that 4×4 ocean grid boxes correspond to 1 potential location of intense mixing. The resulting shapes of the four domains are shown in Figure A.3 of Appendix A. We apply our method to each domain, for a period of time of 19 hours: this allows us to obtain ~ 50 evaluations of the model for each experiment. The results of these experiments are summarized in Table 3.1.

TABLE 3.1: Comparison between different search regions: the columns indicate, from left to right: the search region, the number of model evaluations completed, the maximum (or initial) value assumed by $f(x)$, the value of $f(x)$ relative to the optimal solution, and the ΔpCO_2 obtained at the end of a 50 year simulation under the conditions defined by x_{opt}
- *values relative to $f(x_{in})$.

| Experiment | # evaluations | $f(x_{max})$ [ppm] | $f(x_{opt})$ [ppm] | ΔpCO_2^{oce} [ppm] |
|------------|---------------|--------------------|--------------------|----------------------------|
| Indian | 56 | 249.2816* | 249.1762 | + 0.05 |
| Pacific | 51 | 249.3806 | 249.1707 | + 0.08 |
| Atlantic | 48 | 249.2176 | 249.1593 | - 0.12 |
| Global | 46 | 249.2080* | 249.1742 | // |

It is important to notice that the improvement in the value of the objective function $f(x)$ is relatively small. This is due to the fact that we are increasing the value of K_v over a restricted area of the ocean: with $n = 3$ mixing hotspots, the area involved in the geoengineering technique would be $\sim 3 \times 10^6$ km². Moreover, we look at the global impact of the local increment in K_v , having defined the objective function $f(x)$ as the global mean value of pCO_2^{oce} : this is necessary, in order to take into consideration both local and non-local effects, which might counter-act each other. Lastly, the value of $f(x)$ is calculated after only 5 years of artificially enhanced mixing.

To check if the effects are amplified after a longer period of time, we consider the configurations indicated by the optimal solutions x_{opt} , and we run 50 years simulations with the OGCM in which artificial mixing is implemented from year 0 to the

end of the run. We compare the variation in the value of the partial pressure of CO_2 at the ocean surface, $\Delta p\text{CO}_2^{\text{occe}}$, in the different experiments.

From this analysis, we can see that the optimization procedure leads to the identification of a configuration that causes a reduction in the value of $p\text{CO}_2^{\text{occe}}$, lying in the Atlantic Ocean domain. The results obtained with the other three domains (Indian, Pacific, and Global Ocean) are similar and less promising than those obtained in the Atlantic Ocean. This can be due to the size of the latter domain (which is smaller than the Pacific and Global Ocean) and on its shape (being narrow in the zonal direction, and reaching high latitudes in both hemispheres).

Therefore, from now on, we will focus on maximizing the efficiency of our method, applying it to the Atlantic Ocean.

We now address the effects linked to the choice of the number of intense mixing sites n : we vary its value, ranging from $n = 2$ to $n = 6$, and compare the evolution of $f(x_{\text{opt}})$ in the different cases. Note that each location is represented by two variables (its model coordinates), therefore the dimension of the problem dim is twice the number of high mixing sites n . Figure 3.3 shows the results of this analysis.

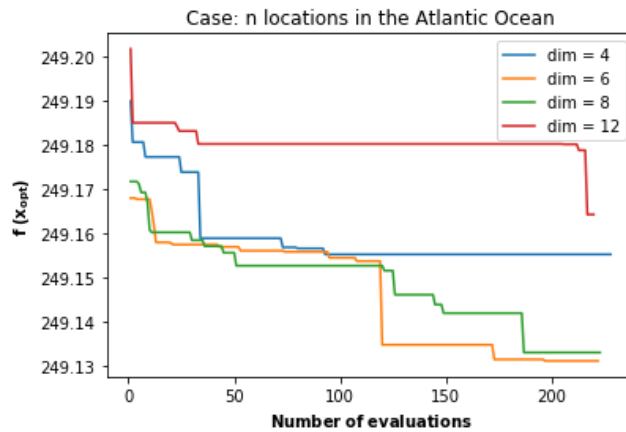


FIGURE 3.3: Comparison of the convergence curves, varying the problem dimension from 4 ($n = 2$ sites of enhanced K_v) to 12 ($n = 6$ sites of enhanced K_v), with the search region illustrated in Figure A.3a (Atlantic Ocean).

As expected, when dim increases, a higher number of evaluations is needed to find a solution close to the optimal. Looking at Figure 3.3, one can observe that the algorithm is not efficient when a too high dimension is set: in the case of $\text{dim} = 2n = 12$, the value of $f(x_{\text{opt}})$ does not improve for more than 150 model evaluations.

One can also note that setting $n = 3$ or 4 leads to a better solution than using $n = 2$: this can be explained by the fact that, with a larger area of the ocean involved in the experiments, the signal is larger and clearer, improving the efficiency of the method.

The objective of this part of the project is to identify the most promising locations where to increase mixing. Therefore, we look at the locations in the Atlantic Ocean domain that most frequently appear in the 20 best feasible solutions, which were found at the end of the optimization procedure with $\text{dim} = 6$ (found in the last ~ 50 model evaluations).

Figure 3.4 shows the number of times that each site is present in those solutions.

Looking at Figure 3.4, the most evident feature is that two cells are almost always found in the best solutions: these cells are located in the Western Equatorial Atlantic, along the coast of South America. The favorable area seems to extend in the northeastern direction, towards the Strait of Gibraltar, and some solutions also contain sites within the Mediterranean Sea. We can conclude that these might be regions where the dominant effects of increasing K_v , at short time-scales of a few years, are changes in the *thermodynamic forcing* (due to the upwelling of colder water to the warm surface layer) or/and in the *biological forcing* (due to the upwelling on nutrients). This conclusion will be verified looking at the results from the CESM simulations, which are presented in the following section.

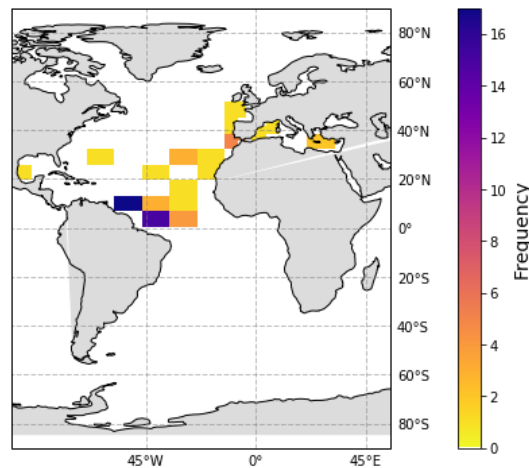


FIGURE 3.4: Frequency of the presence of each location in the 20 best feasible solutions, which were found applying the optimization procedure to the Atlantic Ocean domain, with $dim = 6$.

3.5 CESM hotspots experiments

Firstly, we use the CESM model to test the effects generated by some of the configurations found while running the optimization model. Note that these were the best solutions found after ~ 50 model evaluations, and better solutions were found when we let the model run for a longer period of time.

The three configurations that we selected can be visualized in Figure 3.5.

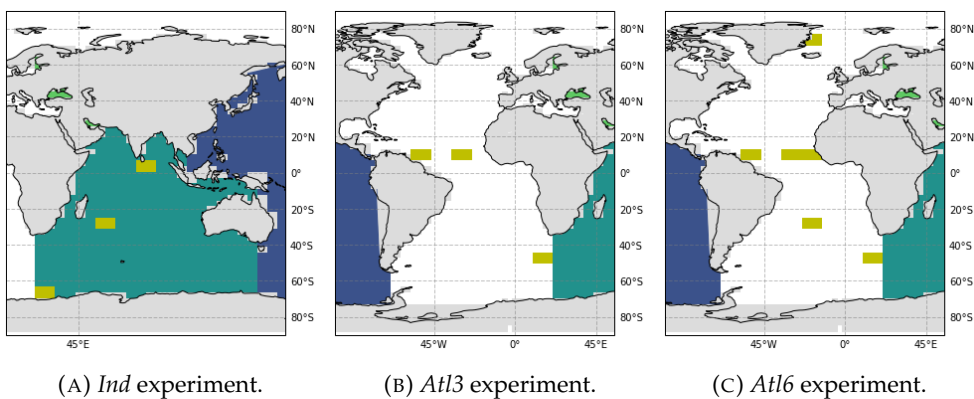


FIGURE 3.5: Maps indicating the locations where K_v is incremented (yellow squares) in the 3 hotspots experiments.

Two configurations (*Ind* and *Atl3* experiments) involve the implementation of 3 hotspots of vertical mixing in the Indian or Atlantic Ocean, while one experiment is conducted with 6 artificial sites (*Atl6* experiment).

The main experiments results are summarized in Figure 3.6. The carbon fluxes to the atmosphere (J_{tot}) are separated into the fluxes from the ocean (J_{oce}) and from land (J_{land}). The surface fluxes are characterized by a strong natural variability on seasonal to interannual time scales: for this reason, Figure 3.6a shows the 5 year running average of the cumulative anomaly between the carbon surface fluxes in the experiment and in the control run. This plot displays 140 years of simulation: at year 40, the simulation branches in four, one control simulation without the employment of artificial mixers, and three simulations where K_v is incremented in the regions defined in Figure 3.5. Looking at the evolution in time of the cumulative anomaly in the CO₂ surface fluxes (Figure 3.6a), we can conclude that, in all the experiments, there is an increase in the amount of carbon released by the ocean to the atmosphere. The land component partially counteracts this effect, since more carbon is stored in the soil and vegetation pools. As a result, the difference between the atmospheric concentration of CO₂ in the CTRL run and the experiment is positive, in general, but the values fluctuate within the variability range registered in the CTRL simulation.

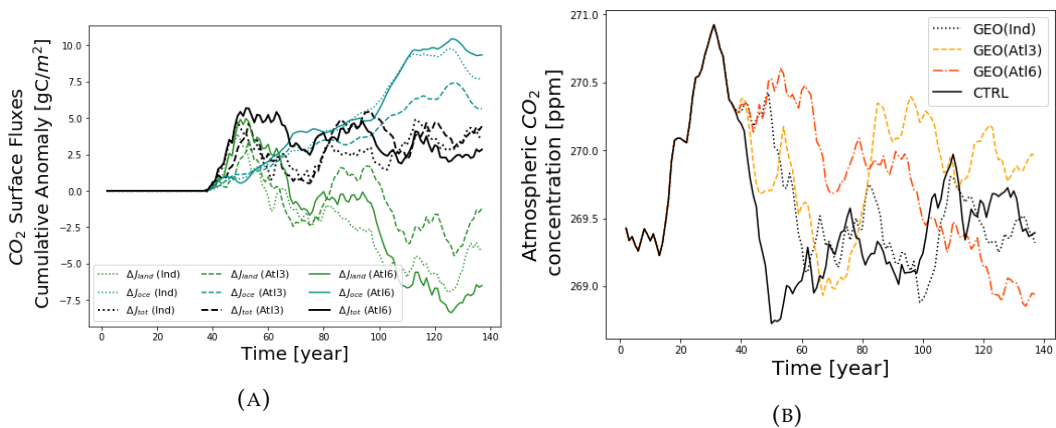


FIGURE 3.6: Evolution in time of the CO₂ surface fluxes cumulative anomaly [g C m⁻²](3.6a) and atmospheric CO₂ concentration [ppm](3.6b) in the 3 hotspots experiments.

The only experiment where a decreasing trend can be detected is *Atl6*: however, simulations over a longer period of time are needed to verify if the trend would continue after 100 years of artificial mixing, and lead to significantly lower atmospheric CO₂ concentrations.

In Figure 3.7 we focus on the *Atl6* experiment, as we want to understand which regions are affected by the largest cumulative anomalies at the end of the simulation.

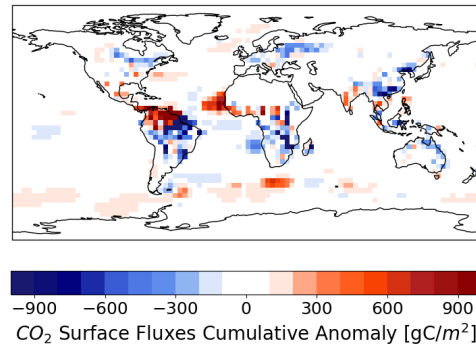


FIGURE 3.7: Distribution of the CO_2 surface fluxes cumulative anomaly [g C m^{-2}] at the end of the 100 year simulation.

Firstly, comparing Figure 3.7 and 3.5c, we can verify that the largest effects are found at some of the sites where K_v is incremented, but not all the hotspots are detectable in the map. The largest growths in the oceanic outgassing of CO_2 are found at the sites of artificial mixing in the Equatorial Atlantic and in the Southern Ocean, while the largest responses by the land component occur in the South American continent.

The drivers of the oceanic and land responses will be analyzed in more detail conducting regional experiments, which are described in the next Section.

3.6 CESM regional experiments

In this Section, we present the results of the two regional experiments conducted with the CESM.

The areas where K_v is incremented in each experiment are indicated by Figure 3.8. Note that the EQATL_MED experiment (Figure 3.8a) was designed using the information obtained from the resolution of the optimal displacement problem: therefore, we expect from this scenario an increase of the oceanic carbon uptake, as projected by the Mk3L-COAL model within the optimization procedure.

We compare this scenario with the NWATL experiment (Figure 3.8b), in which we test the sensitivity of the Atlantic Meridional Overturning Circulation (AMOC) to variations in K_v in the Northwestern Atlantic Ocean, and the potential effects on the carbon cycle.

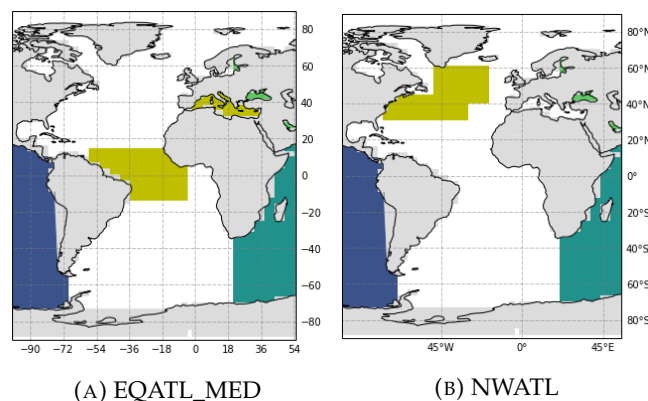


FIGURE 3.8: Maps indicating the locations where K_v is incremented (yellow squares) in the 2 regional experiments.

Table 3.2 contains the cumulative anomalies in the surface carbon fluxes, separating the total flux to the atmosphere (J_{tot}) into the surface flux from the ocean (J_{oce}) and from the land component (J_{land}). Moreover, we consider how the variations evolve from the beginning of the experiment, evaluating the cumulative anomaly over the first 5 years of artificial mixing, to the end of the simulation (after 100 years of enhanced mixing).

TABLE 3.2: Changes in the surface carbon fluxes, expressed as the cumulative anomaly [gC/m^2] between the control run CTRL and each experiment (EQATL_MED and NWATL) over the first 5 and 100 years of the implementation of artificial mixing in the two regional experiment.

| Experiment | Surface Fluxes | Cum. An. (gC/m^2) | |
|------------|-------------------|-----------------------|----------|
| | | Year 5 | Year 100 |
| EQATL_MED | ΔJ_{land} | 5.30 | 0.15 |
| | ΔJ_{oce} | -0.52 | 4.79 |
| | ΔJ_{tot} | 4.78 | 4.94 |
| NWATL | ΔJ_{land} | 1.29 | -2.05 |
| | ΔJ_{oce} | 1.41 | 12.29 |
| | ΔJ_{tot} | 2.69 | 10.24 |

Note that, over the first five years of the EQATL_MED experiment, we obtain $\Delta J_{oce} = -0.52 < 0$, meaning that the surface flux from the atmosphere to the ocean increases on these time scales: this confirms the results of the optimization problem, which aimed at increasing the oceanic carbon uptake on these timescales. However, the total flux to the atmosphere is always higher in the experiment than it is in the CTRL run: initially, this is due to an increased flux of CO_2 from land, while later in time the outgassing from the ocean is dominant.

In the NWATL, the variation in ΔJ_{oce} is responsible for the increase of ΔJ_{tot} by the end of the simulation, while the response of the land component has a dampening effect.

The variations in global mean pCO_2^{oce} , global mean atmospheric CO_2 concentrations and AMOC index are listed in Table 3.3. The AMOC index is defined as the maximum overturning streamfunction, between $z = 500$ m and $z = 3000$ m, at a latitude of 30° N.

TABLE 3.3: Mean values and standard deviations of: the reference values in the CTRL run; the differences between each regional experiment and the CTRL run in global mean pCO_2^{oce} , global mean atmospheric CO_2 concentration and AMOC index, averaged over the last 50 years of simulation.

| Variable | Unit | CTRL mean value | Mean Difference | |
|---------------|------|-------------------|------------------|------------------|
| | | | EQATL_MED | NWATL |
| pCO_2^{oce} | ppm | 266.03 ± 0.63 | $+5.03 \pm 1.06$ | $+1.20 \pm 0.73$ |
| CO_2^{atm} | ppm | 269.49 ± 0.37 | $+3.39 \pm 0.70$ | $+0.32 \pm 0.50$ |
| AMOC index | Sv | 10.88 ± 0.84 | $+1.38 \pm 1.09$ | -4.42 ± 1.51 |

The mean global $p\text{CO}_2^{\text{occe}}$ increases in both regional experiments by the end of the simulations. However, note that at the beginning of the EQATL_MED experiment its value decreases, with a variation of -0.94 ppm after the first 2 years of increased K_v .

We also look at the effect on the MOC strength, analysing the changes in the AMOC index. As we anticipated, increasing K_v in the Northwestern Atlantic causes a large response from the meridional circulation: however, in contrast to what expected, the sign of the AMOC index variation is negative, indicating a significant reduction in the strength of the circulation.

In the following paragraphs, we will analyse in more detail the mechanisms leading to these results, looking first at the EQATL_MED experiment (Section 3.6.1), and then at the NWATL experiment (Section 3.6.2).

3.6.1 Increased K_v in the Equatorial Atlantic and Mediterranean Sea

In this paragraph, we focus on the effects of increasing K_v in the Equatorial Atlantic and Mediterranean Sea (EQATL_MED experiment).

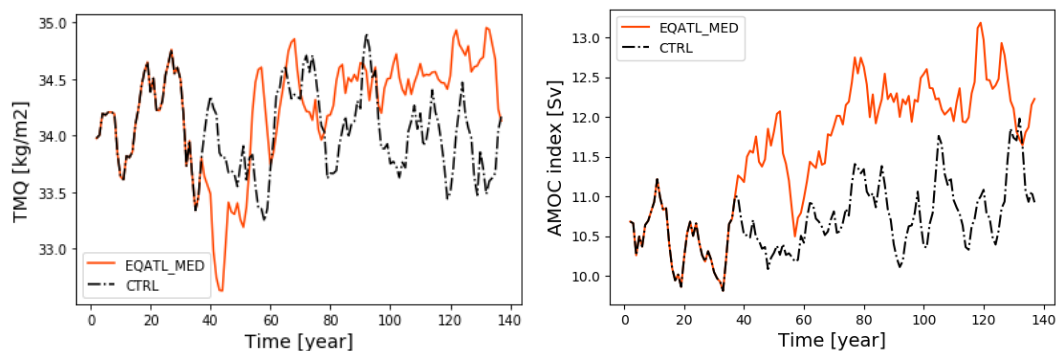
Figure B.8a shows how the land and oceanic carbon fluxes varied as a response to the enhancement of vertical mixing.

Two phases can be clearly identified looking at Figure B.8a.

In the first phase, the oceanic uptake increases: the reasons for this achievement can be understood looking at Figure 3.10, which shows the evolution in time of the mean profiles of temperature and POC production in the Atlantic Ocean. One can see that both the *thermodynamic* and *biological forcings* appear to be responsible for a higher oceanic carbon uptake: at the ocean surface, we can detect lower SST and higher POC production already after 1 year of mixing enhancement.

However, in the first years of employment of artificial mixers, the dominant effect is linked to the outgassing of CO_2 from land.

The reason for this outgassing is associated to drier conditions over the Amazonian forest in the first decade of artificial mixing. This phenomenon can be deduced looking at Figure 3.9a, which illustrates the evolution in time of the total (vertically integrated) precipitable water (TMQ) over this region.



(A) Evolution in time of the total (vertically integrated) precipitable water [kg m^{-2}] over the region of the Amazonian forest.

(B) Evolution in time of the AMOC index [Sv].

FIGURE 3.9: EQATL_MED: the quantities shown in the plots are running averages over 5 years of the relative variables.

Shortly after year 40, when the simulation branches in CTRL run and EQATL_MED experiment, it is possible to see that the TMQ reaches a minimum value, which is below the range of natural variability observed in the control simulation. This is a consequence of lower sea surface temperature (see the vertical profile of temperature after 1 year, Figure 3.10a), caused by the increase in the upwelling of colder water from deeper layers. The cooling of the upper levels leads to variations in the evaporation fluxes and zonal wind pattern, which likely explain the lower TMQ values over the South American continent.

Later in time, the temperature profile evolution (Figure 3.10a) shows a significant warming in the whole water column, with an increase of almost 2°C at $z = 200\text{ m}$ after 100 years of artificial mixing. This explains both the increase in TMQ and in the carbon fluxes from the ocean, observed in the second phase of the experiment. The warming is localized in the area where K_v is increased, as it is a direct consequence of the higher ventilation in the upper 1000 m of the Equatorial Atlantic Ocean. Note that the observed warming at low latitudes is not due to a weaker Atlantic Meridional Overturning Circulation (see Table 3.3 and Figure 3.9b).

In the last period of the simulation, the roles of the two components are reversed, with the land component absorbing more atmospheric CO_2 than in the control run by the end of the simulation. The cumulative anomaly in the CO_2 surface fluxes at the end of the simulation is shown in Figure B.8b. Looking at this Figure, one can see that the strongest sink of atmospheric CO_2 at the end of the simulation is found in the Amazonian region, while the strongest oceanic source region is in the Equatorial Atlantic. Therefore, we can conclude that, after 100 years of artificial mixing in these regions, the dominant effects are due to the thermodynamic forcing (lower solubility of CO_2 due to higher water temperatures). Note that, at the end of the simulation, the POC production is about 4 times higher, on average, at the surface of the Atlantic Ocean (see Figure 3.10b), with the strongest enhancement being found in the Mediterranean Sea: this can indicate an increase in the sinking of carbon, linked to higher nutrient availability in the upper layers and, as a result, to a more efficient biological pump. However, this improvement is not high enough to compensate for the reduction in the efficiency of the solubility pump, due to a warmer oceanic upper layer and stronger upwelling of DIC.

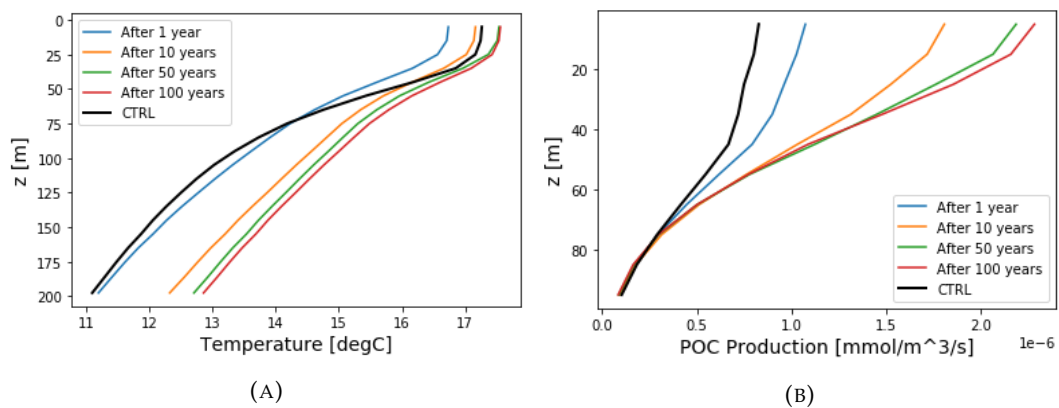


FIGURE 3.10: Evolution in time of the vertical profiles of temperature [$^{\circ}\text{C}$] (3.10a) and POC production [$\text{mmol m}^{-3} \text{s}^{-1}$] (3.10b) in the EQATL_MED experiment, averaged over the Atlantic Ocean, and compared with the mean profiles in the CTRL run.

3.6.2 Increased K_v in the Northwestern Atlantic

Lastly, we focus on the results from the NWATL experiment.

In Figure B.9a, we can see the evolution in time of the carbon surface fluxes cumulative anomaly. The dominant response is the continuous outgassing of CO_2 from the ocean, caused by the increase in $p\text{CO}_2^{\text{oce}}$ (see Table 3.3). This effect is partially compensated by an increase in the carbon uptake by the land component.

The relevant variations in the surface fluxes are mainly occurring over two regions: in the ocean, the flux to the atmosphere increases in the North Atlantic, while the carbon uptake from land increases in the Amazonian region.

Increasing K_v in the North Western Atlantic, the atmospheric response leads to a systematic increase in the precipitation flux over this region, as it is shown in Figure 3.11b. The freshwater input anomaly in the North Atlantic can trigger a feedback mechanism, causing a decline in the AMOC strengths. Looking at Figure 3.11a, it is possible to observe that the AMOC index decreases steadily during the simulation, with an instantaneous response at year 40, when the artificially enhanced mixing starts.

A weaker AMOC reduces the efficiency of the solubility pump: this explains why the strongest oceanic source of CO_2 to the atmosphere in the experiment is found in the North Atlantic (Figure B.9b). Warmer sea surface temperatures at lower latitudes, on the other hand, are the likely reason for the increase in the carbon uptake in the Amazonian region, similarly to what has been observed in the EQATL_MED experiment.

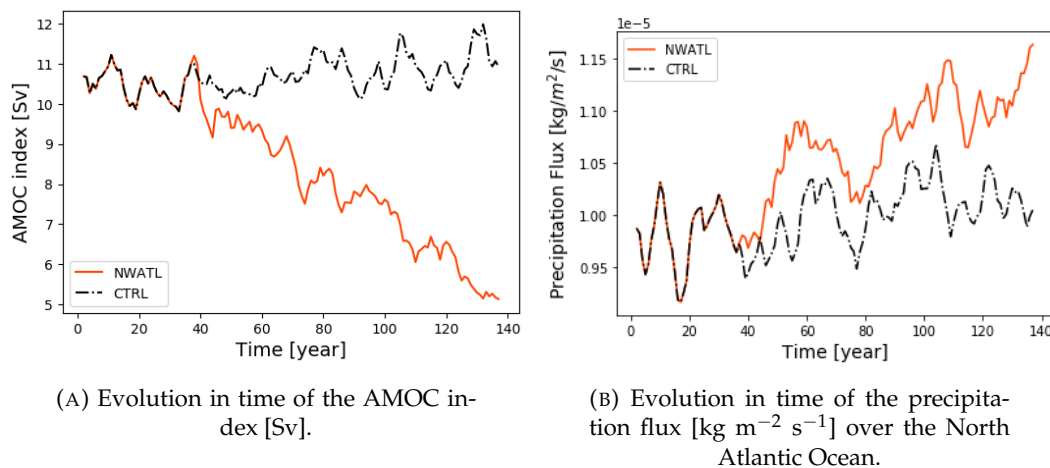


FIGURE 3.11: NWATL experiment: the quantities shown in the plots are running averages over 5 years of the relative variables.

Chapter 4

Discussion

4.1 Estimate of the power required to increase K_v

Using the OGCM included in the CSIRO Mk3L-COAL model, we found that, on average, 7.7 kW km^{-2} are added to the system to increase K_v from the ocean surface to a depth of 1000 m. Considering that the total area involved in the regional experiments with CESM is $\sim 1 \times 10^7 \text{ km}^2$, then the total power necessary for the implementation of these configurations would be about 77 GW.

In order to avoid an increase in the energy demand due to the implementation of this technique, we can imagine to extract power from ocean currents: this would be a clean, local, renewable energy source, with the potential of supplying 75 GW when we consider the Gulf Stream alone, according to the US Energy Department (*Ocean Energy*).

However, large uncertainties characterise the attempts to evaluate the amount of energy that can be extracted from ocean currents, since the available ocean turbines have important technical limits at the moment: in particular, each technology is developed to work at a specific range of depth and mean peak velocity.

The large energy demand could represent a limit for the implementation of any mechanical geoengineering method, since the cost of application would be elevated and they will have to be compensated by the mitigation of climate change.

In this project, we also observed that the total power needed to generate a mixing hotspots can be reduced, for example, by varying the range of depth at which K_v is implemented. If artificial mixing starts from $z = 200 \text{ m}$ and reaches $z = 1000 \text{ m}$, the power needed would be, on average, 3.2 kW km^{-2} , with a reduction of almost 60 % compared to the experiment starting from the surface of the ocean.

Therefore, future studies can try to optimize the implementation of mechanical geoengineering method, by taking into account not only the oceanic response, but minimizing the required power and economic costs.

Moreover, the optimization procedure can be improved, in order to identify the minimum areas of the ocean where artificial mixers must be employed to significantly reduce the atmospheric CO_2 concentrations, maximizing the benefit linked to the mitigation of climate change. This point will be further discussed in the following Section.

4.2 Optimization procedure

In this project, we developed an optimization procedure to identify the locations where a constant increase in K_v would lead to the largest reduction in the global mean $p\text{CO}_2^{\text{oce}}$. As discussed in Section 3.4, a preliminary analysis led to a focus on the Atlantic Ocean, since it emerged as the domain where the largest reduction in the

global mean pCO_2^{oce} was found, within a limited number of model evaluations (see Table 3.1). It would be interesting to deepen the analysis on the other domains during future studies: in particular, the global experiments conducted with the CSIRO climate model (Section 3.2) indicated that some of the largest, beneficial effects were observed in the Pacific Ocean, for example along the western coasts of North and South America. Moreover, other degrees of freedom could be introduced in the problem, allowing for variations in the strength, sign and range of the K_v increment, in order to optimize these problem variables.

Lastly, our results from the CESM simulations highlighted the importance of taking into account the atmospheric and land responses in the optimization procedure: in fact, on decadal time-scales, the evolution of the Earth System response to this perturbation is dominated by the variation in the precipitation pattern. Therefore, the optimization algorithm should be coupled to an Earth System Model, allowing to define as objective function a climate metric that combines all the relevant quantities, in particular the variation in pCO_2^{atm} . Additional constraints can be introduced to take into account the power added to the global ocean, the economic cost of the implementation, and even the environmental impact of the method.

Chapter 5

Conclusion

In this project, we explored the potential of creating artificial sites of enhanced diapycnal mixing to increase the oceanic carbon uptake. This method would represent an opportunity to implement an ocean-based mechanical geoengineering technique, affecting both the biological and the solubility pumps.

Using the OGCM included in the CSIRO Mk3L-COAL model, we found that approximately 7.7 kW km^{-2} are added to the system to increase K_v from the ocean surface to a depth of 1000 m. The resulting variation in the global mean $p\text{CO}_2^{\text{oce}}$ is positive, but we observed reductions of this quantity over specific regions of the ocean. We designed an optimization procedure to obtain a negative variation in the global mean $p\text{CO}_2^{\text{oce}}$, and to maximize the magnitude of this reduction, by coupling the OGCM with the NOMAD software. A preliminary analysis led us to focus on the Atlantic Ocean. Using this domain, the optimization algorithm was proved to be more efficient than using other search regions, and we individuated two regions where an increase in K_v would lead to a reduction in the global mean $p\text{CO}_2^{\text{oce}}$: the Equatorial Atlantic and the Mediterranean Sea. Testing this configuration with the CESM, the fully coupled model confirmed the sign of the response from the air-sea CO_2 flux on the short time scales, with $\Delta J_{\text{oce}} = -0.52 \text{ gC m}^{-2}$ after 5 years of enhanced vertical mixing. The increase in the oceanic carbon uptake can be attributed to the thermodynamic and biological forcing, since the first years of the experiment are characterized by lower mean SST and higher POC production rates in the basin. However, the global mean atmospheric CO_2 concentration in the second half of the 100 years experiment increases by $3.4 \pm 0.7 \text{ ppm}$. The reason for the increase, initially, is associated with the outgassing of CO_2 by the terrestrial component, linked to the effect that the variation of the temperature profile in the Atlantic Ocean has on the precipitation pattern over South America. On longer timescales, the higher atmospheric CO_2 concentrations are maintained by a reduction in the solubility of carbon at the ocean surface, due to warmer temperatures at low latitudes. After 100 years of artificial mixing, the POC production is about 4 times higher, on average, at surface of the Atlantic Ocean; however, the increase in carbon sinking is not high enough to compensate for the reduction in the efficiency of the solubility pump.

Similarly, in all the other configurations that we tested with the CESM, the dominant responses on short time scales were linked to the effect of changes in the sea surface temperature on the atmospheric processes. In particular, when a higher K_v is simulated in the Northwestern Atlantic, a variation in the freshwater input leads to a constant decline of the AMOC strength, causing a reduction in the efficiency of the solubility pump. For this reason, the global mean $p\text{CO}_2^{\text{oce}}$ increases by 1.2 ± 0.7 , on average, over the last 50 years of simulation.

Future studies should include the atmospheric and land responses in the optimization procedure, in order to identify the configurations that lead not only to an

increase the efficiency of the oceanic carbon pumps, but to an increase in the net surface carbon flux from the atmosphere to the ocean and land components.

Appendix A

The optimization problem

In this Appendix, we present in more detail the methods that we use to solve the optimization problem, in which we aim to find the locations where an increase in vertical mixing leads to a reduction in the global mean pCO_2^{gce} .

In order to do so, the OGCM of the CSIRO Mk3L climate model is coupled with the Nonlinear Optimization by Mesh Adaptive Direct Search (NOMAD) software, which is an implementation of the Mesh Adaptive Direct Search (MADS) algorithm (Le Digabel et al., 2009). The MADS algorithms are developed from the Generalized Pattern Search (GPS) class (Audet and Dennis, 2006), which solve optimization problems without computing or explicitly approximate derivatives: therefore, these algorithms are classified as Derivative-Free Optimization (DFO) methods (Torczon, 1997).

In the following paragraphs, we describe the MADS algorithm that is implemented in the NOMAD software, and how we apply it for the resolution of our optimization problem.

A.1 The MADS algorithm

In this Section, we summarize the most important definitions and properties of the MADS algorithm, which is introduced in Audet and Dennis, 2006.

At each iteration k , the goal of the algorithm is to improve the current best solution $x_k \in \Omega$, by finding a solution x_{k+1} such that $f(x_{k+1}) < f(x_k)$, having defined the *objective function* $f : \Omega \rightarrow \mathbb{R}$. To achieve this result, the method carries out a *SEARCH step*. If this first phase is not successful, a *POLL step* follows. The third and last step consists in the update of the current problem parameters. During the first and second steps, the blackbox is evaluated at trial points lying on a discrete space of variable: this structure is called *mesh* and it is defined by

$$M_k = \bigcup_{x \in V_k} \{x + \Delta_k^m Dz : z \in \mathbb{N}^{n_D}\} \quad (\text{A.1})$$

where:

- $\Delta_k^m \in \mathbb{R}_+$ is the mesh size parameter. The minimal mesh size is set to 1 in case of integer variables, as it is in our applications.
- V_k is the set of points already chosen to evaluate the blackbox before iteration k . The software stores all the information from previous iterations, and no double evaluations occur.
- D is the set of mesh directions, i.e. a matrix representing a fixed finite set of n_D directions in the domain. Therefore, the dimension of D is $2n \times n_D$, where $2n$ is the dimension of the problem.

The difference between the *SEARCH* and *POLL* steps lies in the degree of liberty allowed to create the trial points.

In the NOMAD implementation of the *SEARCH* step, many different strategies can be chosen, such as the Variable Neighborhood Search (VNS) (Audet, B  chard and Le Digabel, 2008) or the Latin Hypercube (LH) Sampling (Tang, 1993). Moreover, the user can choose between quadratic models or models provided by the surrogate library to determine the search strategy (see Section A.2).

The flexibility allowed in the *SEARCH* step is motivated by the fact that the convergence analysis does not rely on it, but on the *POLL* step. To guarantee this, the set of poll trial points is defined as:

$$P_k = \{x_k + \Delta_k^m d : d \in D_k\} \subset M_k \quad (\text{A.2})$$

with the following bound:

$$\Delta_k^m \|d\| \leq \Delta_k^p \max \{\|d'\| : d' \in D\} \quad (\text{A.3})$$

where Δ_k^p is the poll size parameter, and D_k is a set of directions. From Equation A.3, we obtain that the distance of the points of P_k to the poll center x_k is bounded above by Δ_k^p . The definitions of D_k and Δ_k^p represent the main developments from GPS to MADS algorithms (Audet and Dennis, 2006): in fact, in the GPS class $D_k \subset D$, while this might not be the case in MADS algorithms. The difference can be visualized looking at Figure A.1.

Figure A.1 shows the three poll strategies already coded in NOMAD. We can see that the GPS is the most rigid option, since it uses the coordinate directions. OrthoMADS directions are still orthogonal, but have greater flexibility: this is the default choice in NOMAD and, in general, it has proven to be the most efficient option (Abramson et al., 2009). The last available technique (LT-MADS) involves randomness in the generation of the directions, using Lower-Triangular (LT) matrices.

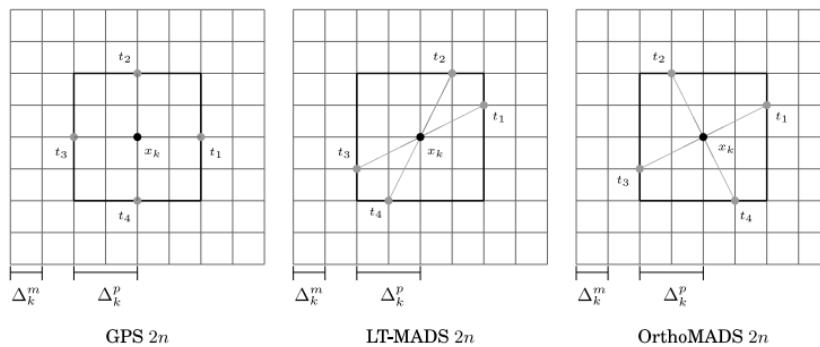


FIGURE A.1: Difference between the GPS, LT-MADS and OrthoMADS in the case $n = 2$, $n_D = 2n$ and $\Delta_k^p = 2\Delta_k^m$ (Le Digabel, 2011).

As a last step of each iteration k , one of the following two options occurs:

1. we found a x_{k+1} such that $f(x_{k+1}) < f(x_k)$, so x_{k+1} will substitute x_k as best feasible solution at the next iteration (*successful iteration*).
2. the iteration was *unsuccessful*: the mesh is refined by reducing Δ_k^m and Δ_k^p to Δ_{k+1}^m and Δ_{k+1}^p .

Note that $\Delta_k^m < \Delta_k^p$ always, and Δ_k^m is reduced faster than Δ_k^p after an unsuccessful iteration. In NOMAD, by default, the initial value of Δ_0^p is calculated from the starting point (given as input), and Δ_0^m is calculated from Δ_0^p .

A.2 SGTELIB library

SGTELIB is the library for dynamic surrogates included in the NOMAD software.

Since the blackbox is computationally expensive to evaluate, the use of computationally cheaper surrogate functions might allow us to find a satisfying solution in a shorter running time.

This library is used in the *SEARCH step*: it sorts the potential search trial points, evaluating them on the surrogate function. After this preliminary analysis, only the most promising points are tested using the blackbox.

The scheme in Figure A.2 illustrates how the surrogate library, the blackbox and the optimization algorithm interact with each other.

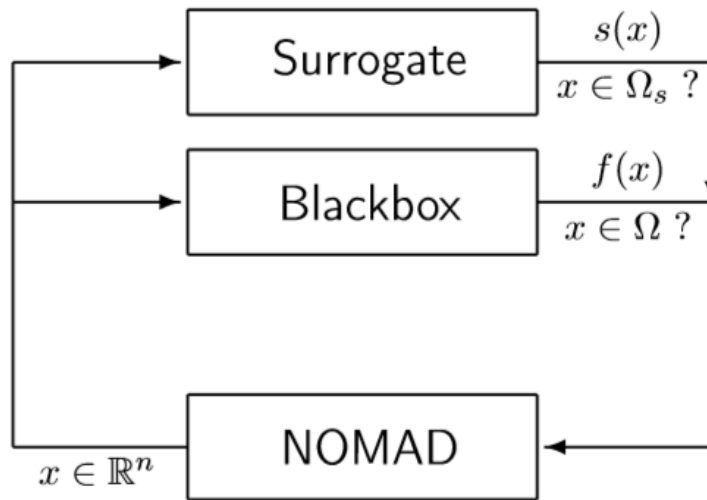


FIGURE A.2: Scheme showing the interaction between blackbox and NOMAD software. The surrogate functions $s(x)$ can be used to simulate the behaviour of the real objective function $f(x)$ (Le Digabel et al., 2009).

A.3 Definition of the optimization problem

We will use the NOMAD software to identify the most promising locations where to artificially increase vertical mixing K_v , as a mean to reduce the atmospheric carbon concentration.

The objective function $f(x)$ that we try to minimize is the global mean partial pressure of CO_2 at the surface of the ocean ($p\text{CO}_2^{\text{oce}}$). The point $x \in \Omega \subset \mathbb{N}^{2n}$ represents the set of coordinates of the n locations where K_v is incremented. Therefore, the dimension of the problem is $\dim = 2n$.

The efficiency of the algorithm depends on the dimension $2n$ of the problem, as well as on the dimension and shape of the search region.

For this reason, we vary the number n of mixing hotspots, and we test four domains, which are shown in Figure A.3.

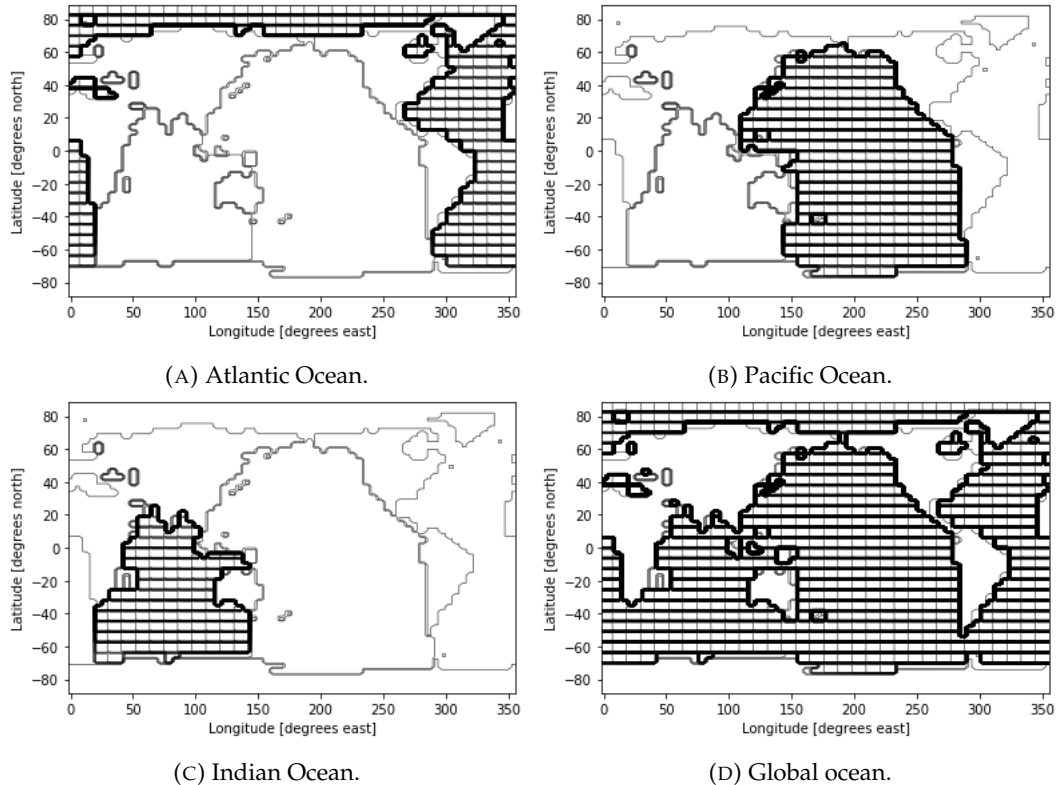


FIGURE A.3: Maps of the four search regions used during the resolution of our optimization problem.

Note that the resolution of the search regions is lower than the resolution of the OGCM, with one potential mixing hotspot extending over 4×4 ocean model columns. This is done to reduce the size of the search region, and reduce the number of evaluations that are necessary to find a satisfying solution.

A.4 The blackbox

At each iteration, the NOMAD software generates a new set of coordinates x , which is given as input to our *blackbox*.

Firstly, the *blackbox* verifies that x lies in the domain Ω . As we can see in Figure A.3, the search regions are highly fragmented, while the NOMAD software can only select the trial points $x = \{x_1, x_2, \dots, x_{2n}\}$ using a lower and upper bound for each variable $x_i, i = 1, \dots, 2n$. Therefore, a trial point can frequently contain locations that are outside the domain, or indicate twice the same location. In order to have exactly n mixing hotspots at each model evaluation, the *blackbox* checks if it is necessary to change a pair of coordinates. If that is the case, the location is moved using a "deterministic spiral walk", similarly to the approaches used to find the optimal solution in a highly fragmented domain in previous studies (Alarie et al., 2013). Firstly, the four neighbouring model grid-cells are tested. If those locations are still not feasible, the radius is extended and the four cells at a distance $r = 2$ from the original location are considered. If no feasible location is found before extending the radius to $r = r_{max}$, a large value is assigned to $f(x)$ without running the ocean model, so that the iteration is automatically unsuccessful.

If $x \in \Omega$, a mask is generated and given as input to run the OGCM for a 5-year simulation. Subsequently, the model output is processed to calculate the global mean pCO_2^{oce} in the last year of the simulation.

One blackbox evaluation is completed in ~ 20 minutes. Note that the computational cost of the blackbox is entirely due to the OGCM simulation, since the generation of the model input and output processing take only a few seconds.

Appendix B

Additional Figures

B.1 Global mixing experiments with the OGCM

We present here the Figures relative to the results discussed in Section 3.2.

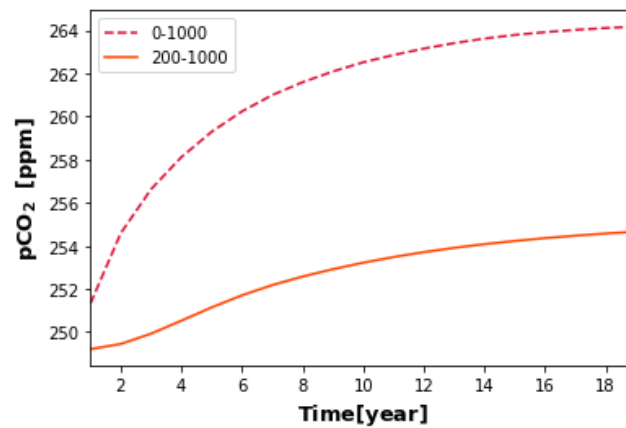


FIGURE B.1: Evolution in time [years from the employment of artificial mixers] of the global mean pCO_2^{oce} [ppm] when K_v is incremented everywhere, from the ocean surface (dashed line) or from $z = 200$ m (solid line), until a depth of 1000 m.

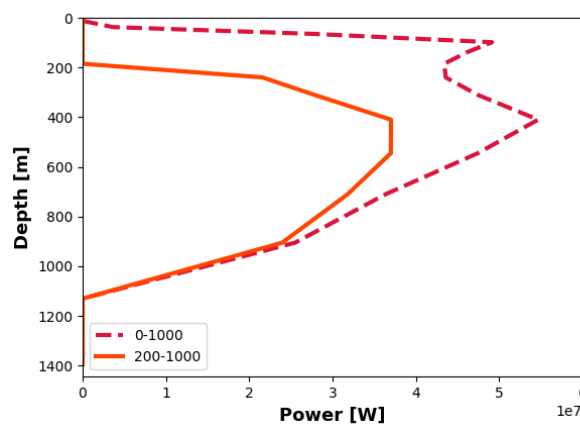


FIGURE B.2: Mean vertical profile of the power [W] added in 1 model column (averaged over 20 years of simulation) when K_v is incremented everywhere, from the ocean surface (dashed line) or from $z = 200$ m (solid line), until a depth of 1000 m.

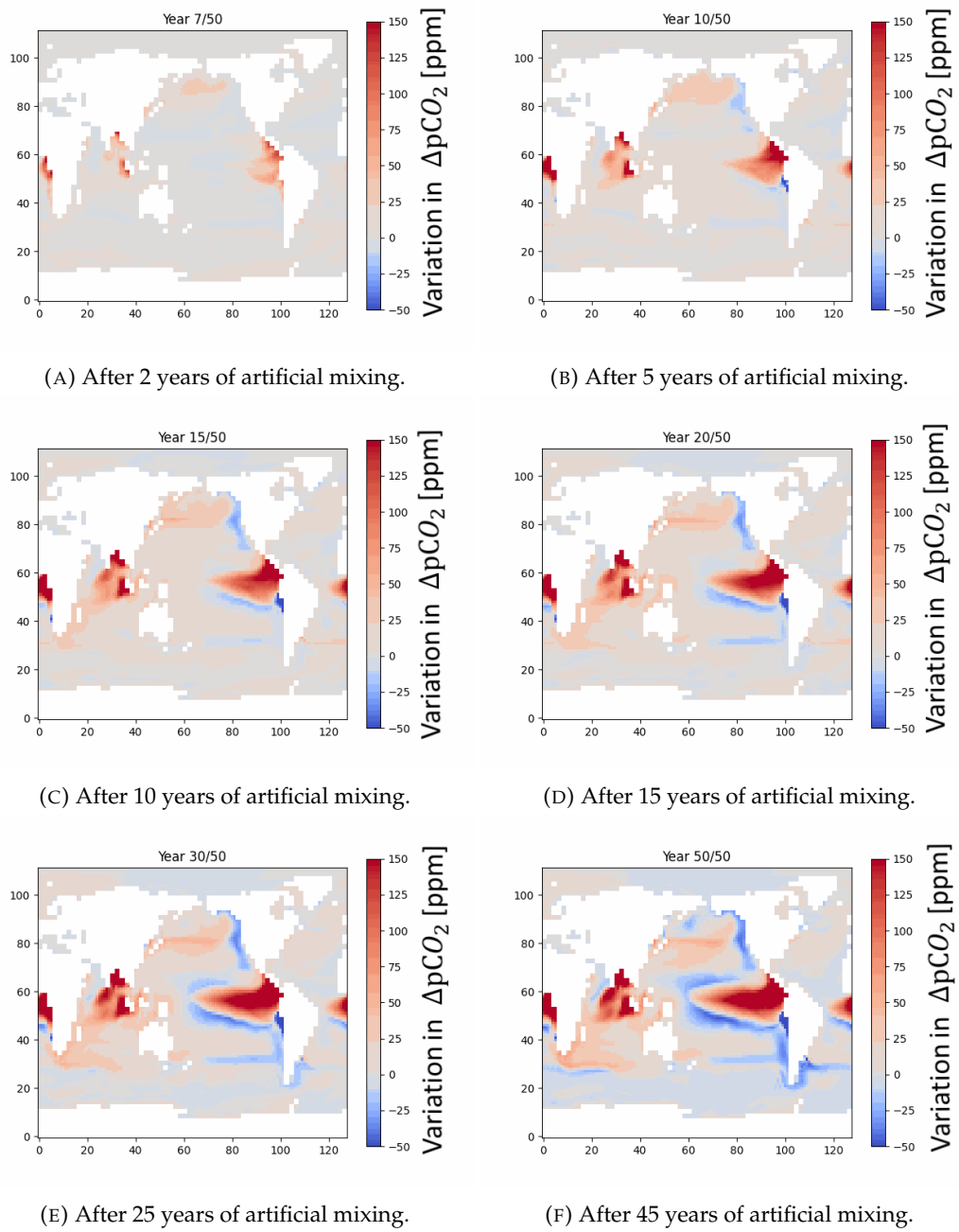


FIGURE B.3: Evolution in time of the distribution of the variation in ΔpCO_2 [ppm] when K_v is incremented everywhere, from $z = 0$ m until $z = 1000$ m.

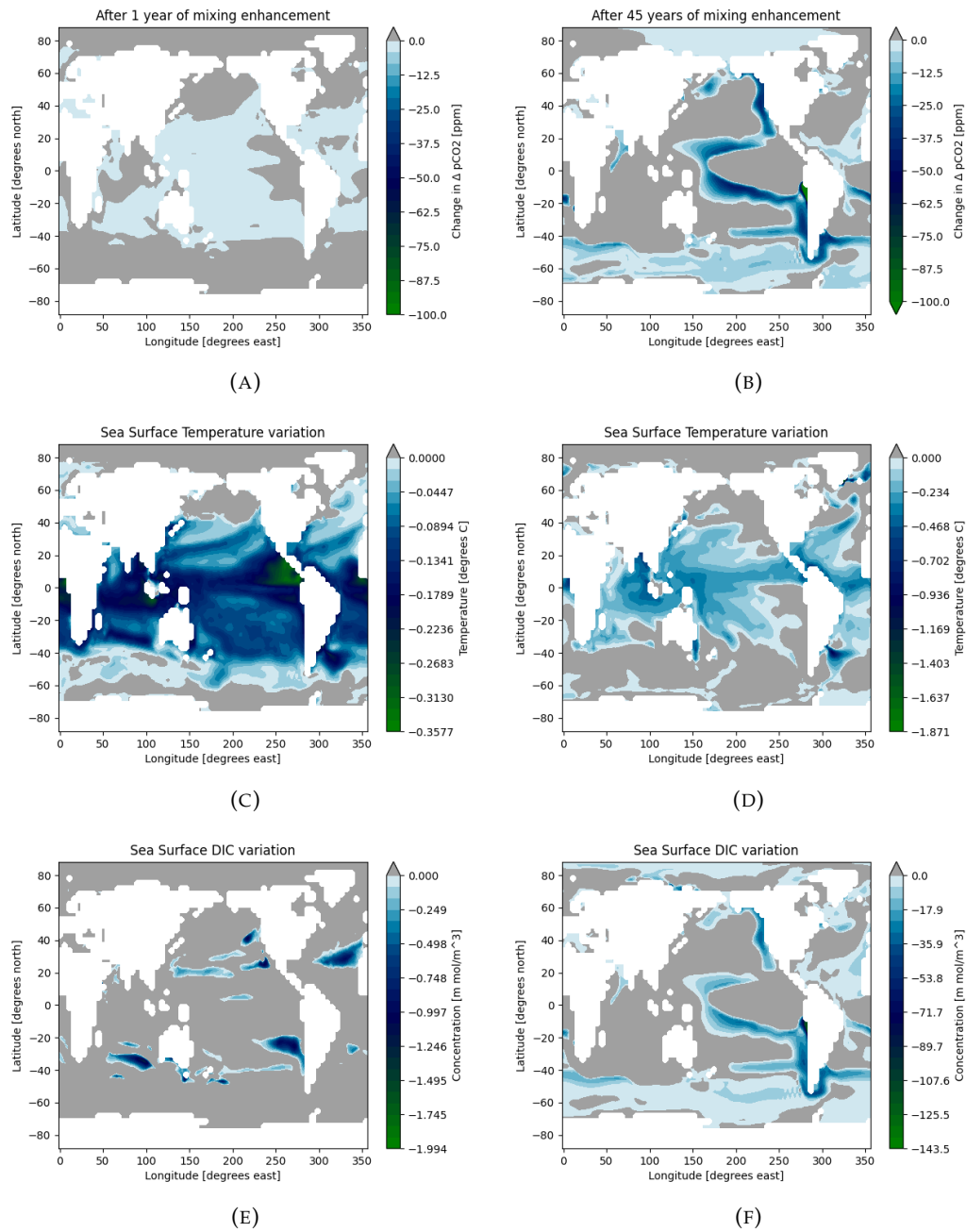


FIGURE B.4: Comparison between the variation in ΔpCO_2 [ppm] (B.4a and B.4b), SST [°C] (B.4c and B.4d) and DIC concentration [mmol m⁻³] (B.4e and B.4f) after 1 year (left column) and after 45 years (right column) of mixing enhancement, at all locations, from $z = 0$ m until $z = 1000$ m. Note that only regions characterized by negative variations are shown, to highlight the areas where the increment of K_v is potentially beneficial for the oceanic carbon uptake.

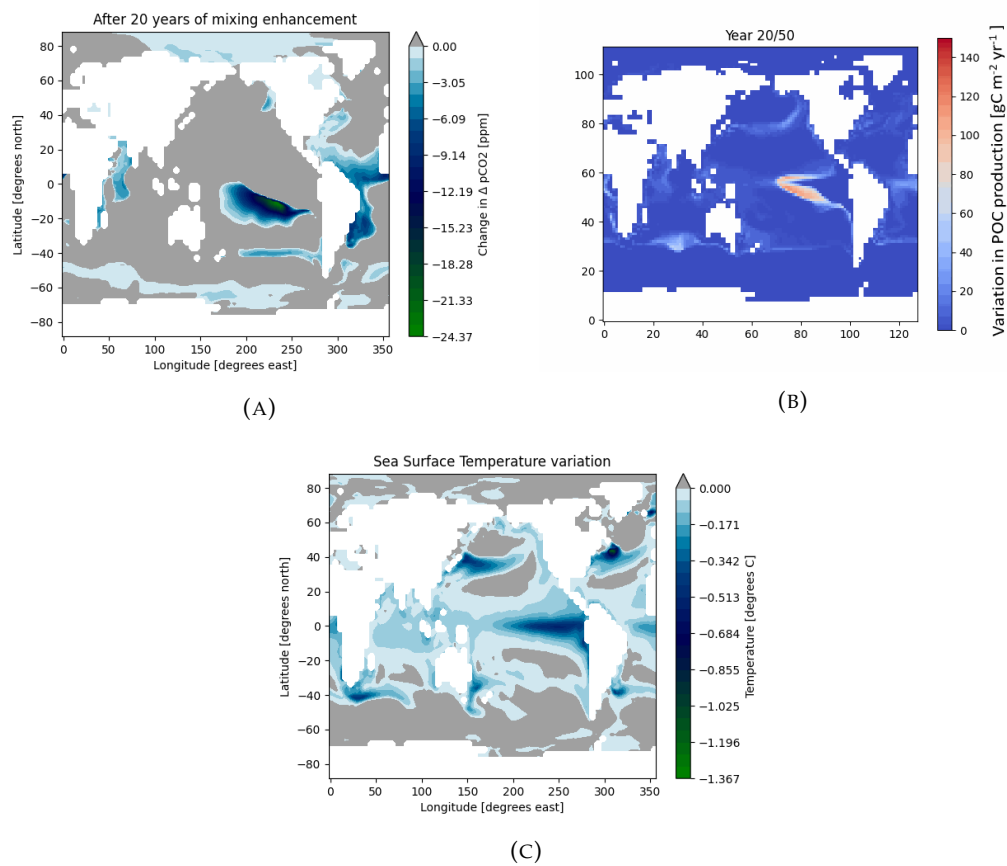


FIGURE B.5: Variation in $\Delta p\text{CO}_2$ [ppm] (B.5a), POC production [$\text{gC m}^{-2} \text{yr}^{-1}$] (B.5b), and SST [$^{\circ}\text{C}$] (B.5c) after 20 years of mixing enhancement, at all locations, from $z = 200$ m until $z = 1000$ m. Note that only regions characterized by negative variations are shown in B.5a and B.5c (only positive variations in B.5b), to highlight the areas where the increment of K_v is potentially beneficial for the oceanic carbon uptake.

B.2 Global hotspots experiments with the OGCM

The following Figures are relative results discussed in Section 3.3.

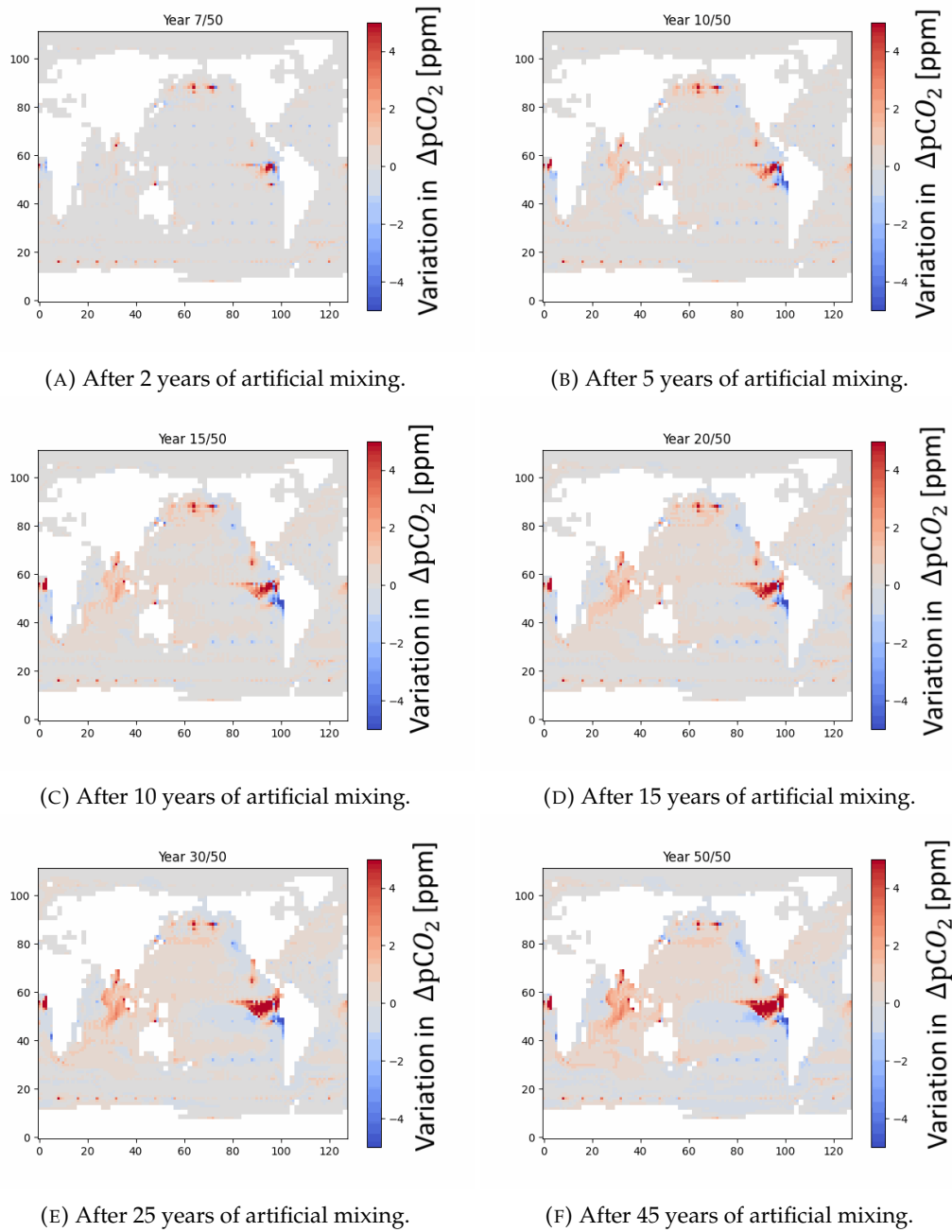


FIGURE B.6: Evolution in time of the distribution of the variation in $\Delta p\text{CO}_2$ [ppm] when K_v is incremented at the locations indicated in Figure 3.2, from $z = 0$ m until $z = 1000$ m.

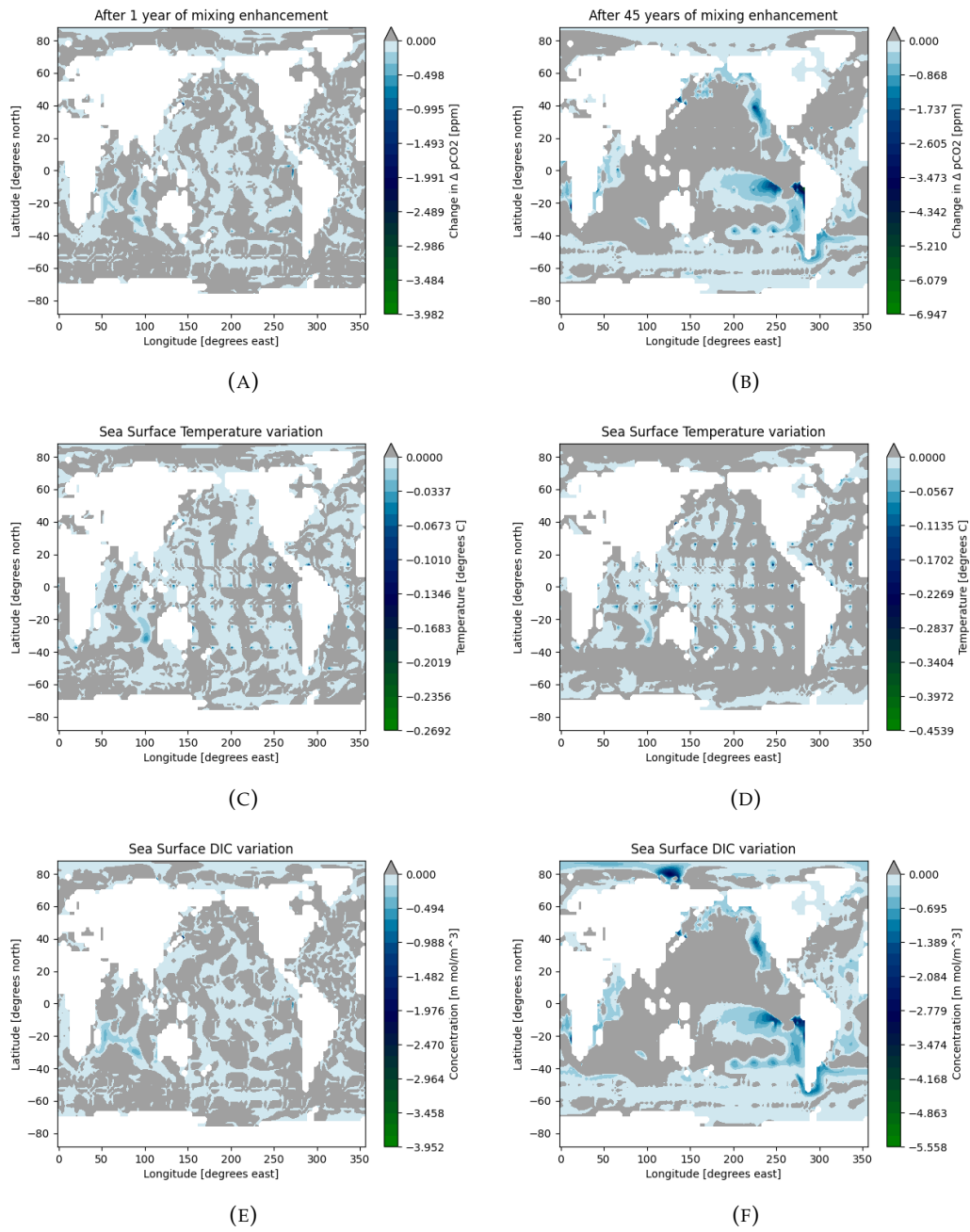


FIGURE B.7: Comparison between the variation in $\Delta p\text{CO}_2$ [ppm] (B.7a and B.7b), SST [°C] (B.7c and B.7d) and DIC concentration [mmol m⁻³] (B.7e and B.7f) after 1 year (left column) and after 45 years (right column) of mixing enhancement, at the locations indicated in Figure 3.2, from $z = 0$ m until $z = 1000$ m. Note that only regions characterized by negative variations are shown, to highlight the areas where the increment of K_v is potentially beneficial for the oceanic carbon uptake.

B.3 CESM simulations: regional experiments

Here we present the Figures described in Section 3.6.

B.3.1 EQATL_MED experiment

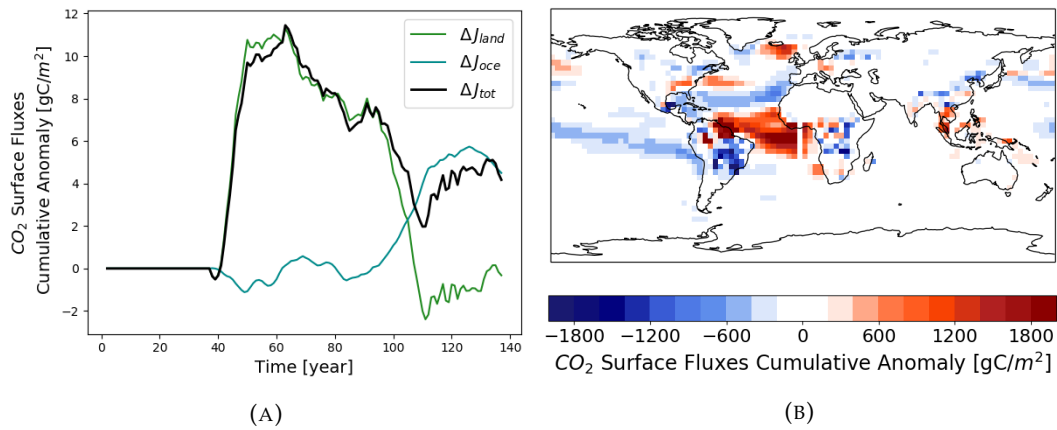


FIGURE B.8: Evolution in time (B.8a) and distribution at the end of the simulation (B.8b) of the CO₂ surface fluxes cumulative anomaly [g C m²] in the EQATL_MED experiment.

B.3.2 NWATL experiment

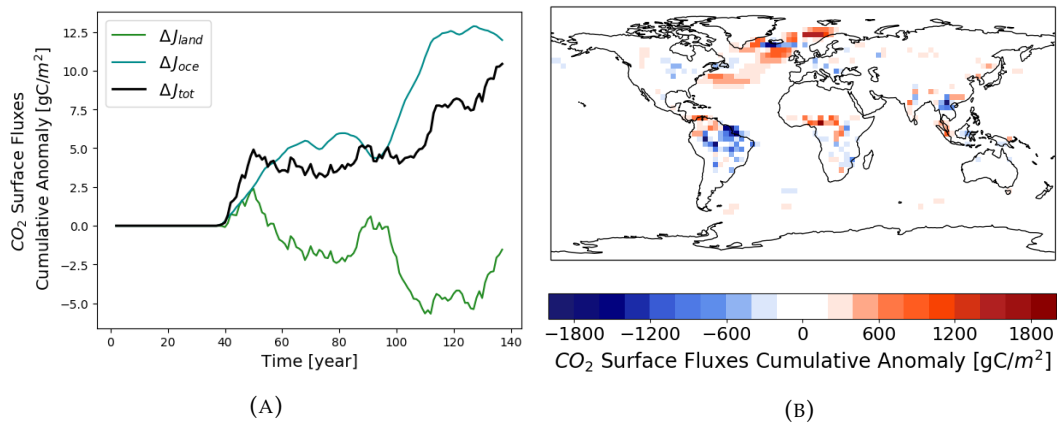


FIGURE B.9: Evolution in time (B.9a) and distribution at the end of the simulation (B.9b) of the CO₂ surface fluxes cumulative anomaly [g C m²] in the NWATL experiment.

Bibliography

- Abramson, Mark A. et al. (Jan. 2009). 'OrthoMADS: A Deterministic MADS Instance with Orthogonal Directions'. In: *SIAM Journal on Optimization* 20.2, pp. 948–966. ISSN: 1052-6234. DOI: 10.1137/080716980. URL: <http://epubs.siam.org/doi/10.1137/080716980>.
- Alarie, Stéphane et al. (2013). 'Snow water equivalent estimation using blackbox optimization'. In: *Pac J Optim* 9.1, pp. 1–21.
- Audet, Charles, Vincent Bécharde and Sébastien Le Digabel (2008). 'Nonsmooth optimization through Mesh Adaptive Direct Search and Variable Neighborhood Search'. In: *Journal of Global Optimization* 41.2, pp. 299–318. ISSN: 09255001. DOI: 10.1007/s10898-007-9234-1.
- Audet, Charles and J. E. Dennis (Jan. 2006). 'Mesh Adaptive Direct Search Algorithms for Constrained Optimization'. In: *SIAM Journal on Optimization* 17.1, pp. 188–217. ISSN: 1052-6234. DOI: 10.1137/060671267. URL: <http://epubs.siam.org/doi/10.1137/060671267>.
- Aumont, O. and L. Bopp (June 2006). 'Globalizing results from ocean in situ iron fertilization studies'. In: *Global Biogeochemical Cycles* 20.2, n/a–n/a. ISSN: 08866236. DOI: 10.1029/2005GB002591. URL: <http://doi.wiley.com/10.1029/2005GB002591>.
- Bluteau, C. E., N. L. Jones and G. N. Ivey (2013). 'Turbulent mixing efficiency at an energetic ocean site'. In: *Journal of Geophysical Research: Oceans* 118.9, pp. 4662–4672. ISSN: 21699291. DOI: 10.1002/jgrc.20292.
- Bryan, K and L J Lewis (1979). 'A Water Mass Model of the World Ocean'. In: 84.8.
- Copin-Montégut, Claire and Milena Bégovic (2002). 'Distributions of carbonate properties and oxygen along the water column (0-2000 m) in the central part of the NW Mediterranean Sea (dyfamed site): Influence of winter vertical mixing on air-sea CO₂ and O₂ exchanges'. In: *Deep-Sea Research Part II: Topical Studies in Oceanography* 49.11, pp. 2049–2066. ISSN: 09670645. DOI: 10.1016/S0967-0645(02)00027-9.
- Dutreuil, S., L. Bopp and A. Tagliabue (2009). 'Impact of enhanced vertical mixing on marine biogeochemistry: Lessons for geo-engineering and natural variability'. In: *Biogeosciences* 6.5, pp. 901–912. ISSN: 17264189. DOI: 10.5194/bg-6-901-2009.
- Fasham, Michael J. R. (2003). *Ocean Biogeochemistry*. Berlin, Heidelberg: Springer Berlin Heidelberg. ISBN: 978-3-642-62691-3. DOI: 10.1007/978-3-642-55844-3. URL: <http://link.springer.com/10.1007/978-3-642-55844-3>.
- Gargett A.E. (1984). 'Vertical eddy diffusivity in the ocean interior.' In: *Journal of Marine Researches* 42, pp. 359–393.
- Jochum, Markus and James Potemra (Dec. 2008). 'Sensitivity of Tropical Rainfall to Banda Sea Diffusivity in the Community Climate System Model'. In: *Journal of Climate* 21.23, pp. 6445–6454. ISSN: 1520-0442. DOI: 10.1175/2008JCLI2230.1. URL: <https://journals.ametsoc.org/jcli/article/21/23/6445/32227/Sensitivity-of-Tropical-Rainfall-to-Banda-Sea>.
- Le Digabel, Sébastien (2011). 'Algorithm 909: NOMAD: Nonlinear optimization with the MADS algorithm'. In: *ACM Transactions on Mathematical Software* 37.4. ISSN: 00983500. DOI: 10.1145/1916461.1916468.

- Le Digabel, Sébastien et al. (2009). 'NOMAD User Guide'. In: *Les cahiers du GERAD* Technical.
- Lozovatsky, Iossif D. (2003). 'Spatial decay of energy density of tidal internal waves'. In: *Journal of Geophysical Research* 108.C6, p. 3201. ISSN: 0148-0227. DOI: 10.1029/2001JC001169. URL: <http://doi.wiley.com/10.1029/2001JC001169>.
- Luo, Yiqi (2007). 'Terrestrial Carbon–Cycle Feedback to Climate Warming'. In: *Annual Review of Ecology, Evolution, and Systematics* 38.1, pp. 683–712. DOI: 10.1146/annurev.ecolsys.38.091206.095808. URL: <https://doi.org/10.1146/annurev.ecolsys.38.091206.095808>.
- Matear, R. J. and A. Lenton (2014). 'Quantifying the impact of ocean acidification on our future climate'. In: *Biogeosciences* 11.14, pp. 3965–3983. ISSN: 17264189. DOI: 10.5194/bg-11-3965-2014.
- Matear, Richard J. and Anthony C. Hirst (1999). 'Climate change feedback on the future oceanic CO₂ uptake'. In: *Tellus, Series B: Chemical and Physical Meteorology* 51.3, pp. 722–733. ISSN: 02806509. DOI: 10.3402/tellusb.v51i3.16472.
- Minesto. *Ocean Energy*. URL: <https://minesto.com/ocean-energy>.
National Oceanographic Data Center, Ocean Climate Laboratory Products.
- Osborn, T. R. (1980). *Estimates of the Local Rate of Vertical Diffusion from Dissipation Measurements*. DOI: 10.1175/1520-0485(1980)010<0083:eotlro>2.0.co;2.
- Oschlies, A. et al. (2010). 'Climate engineering by artificial ocean upwelling: Channelling the sorcerer's apprentice'. In: *Geophysical Research Letters* 37.4, pp. 1–5. ISSN: 00948276. DOI: 10.1029/2009GL041961.
- Phipps, Steven J. (2010). *The CSIRO Mk3L climate system model v1.2*, pp. 1–122. ISBN: 9781921197048.
- Pingree, R.D. and A.L. New (Feb. 1995). 'Structure, seasonal development and sunglint spatial coherence of the internal tide on the Celtic and Armorican shelves and in the Bay of Biscay'. In: *Deep Sea Research Part I: Oceanographic Research Papers* 42.2, pp. 245–284. ISSN: 09670637. DOI: 10.1016/0967-0637(94)00041-P. URL: <https://linkinghub.elsevier.com/retrieve/pii/096706379400041P>.
- Pörtner, Hans-Otto et al. (2019). 'The Ocean and Cryosphere in a Changing Climate. A Special Report of the Intergovernmental Panel on Climate Change'. In: *Intergovernmental Panel on Climate Change*, pp. 1–765. URL: <https://www.ipcc.ch/srocc/chapter/summary-for-policymakers/>.
- Riebesell, Ulf, Arne Kö Rtzinger and Andreas Oschlies (2009). 'Sensitivities of marine carbon fluxes to ocean change'. In: *Proceedings of the National Academy of Sciences of the United States of America* 106.49, pp. 20602–20609. ISSN: 00278424. DOI: 10.1073/pnas.0813291106.
- Rogelj, Joeri et al. (2018). 'IPCC 2018, cap2'. In: *Global warming of 1.5°C. An IPCC Special Report [...]*, p. 2.
- Smith, R et al. (2010). 'The Parallel Ocean Program (POP) reference manual: Ocean component of the Community Climate System Model (CCSM)'. In: *Rep. LAUR-01853* 141, pp. 1–141. URL: <http://nldr.library.ucar.edu/repository/collections/OSGC-000-000-000-954>.
- Takahashi, Taro et al. (1993). 'Seasonal variation of CO₂ and nutrients in the high-latitude surface oceans: A comparative study'. In: *Global Biogeochemical Cycles* 7.4, pp. 843–878.
- Tang, Boxin (Dec. 1993). 'Orthogonal Array-Based Latin Hypercubes'. In: *Journal of the American Statistical Association* 88.424, pp. 1392–1397. ISSN: 0162-1459. DOI: 10.1080/01621459.1993.10476423. URL: <http://www.tandfonline.com/doi/abs/10.1080/01621459.1993.10476423>.

- Torczon, Virginia (1997). 'On the convergence of pattern search algorithms'. In: *SIAM Journal on Optimization* 7.1, pp. 1–25. ISSN: 10526234. DOI: 10.1137/S1052623493250780.
- Zhang, Zhihua et al. (Sept. 2015). 'Review of geoengineering approaches to mitigating climate change'. In: *Journal of Cleaner Production* 103, pp. 898–907. ISSN: 09596526. DOI: 10.1016/j.jclepro.2014.09.076. URL: <https://linkinghub.elsevier.com/retrieve/pii/S0959652614010154>.